Physics – Uspekhi **55** (3) 270 – 300 (2012)

INSTRUMENTS AND METHODS OF INVESTIGATION PACS numbers: **07.78.+s**, 78.70.Bj, 81.16.Ta, **81.40.–z**

Application of micro- and nanoprobes to the analysis of small-sized 3D materials, nanosystems, and nanoobjects

A D Pogrebnjak, A G Ponomarev, A P Shpak, Yu A Kunitskii

DOI: 10.3367/UFNe.0182.201203d.0287

Contents

Abstract. The basic physics behind the interaction of ions with solid-state matter is discussed, with an emphasis on the formation of interaction products between the ions and target atoms. Processes covering modification of high-resistance materials for use in small-sized 3D structure technology are described. Current trends in and problems facing the development of the scanning nuclear microprobe (SNMP) are reviewed. The application of slow positrons to diagnosing materials is examined and the techniques of positron microscopy and microprobing are presented. The potential of near-field microwave microscopy for diagnosing superconducting ceramics and of microwave microscopy for nanotechnology applications are assessed. The examples given include the use of micro- and nanoprobes to analyze nanoobjects (such as green algae cells with 3D-distributed microelements, etc.), to develop the topological aspects of integrated microcircuits in nanoelectronics, and some other applications. The role of iron in pathogenesis of Parkinson's disease is highlighted, the latter being the subject of research in neurochemistry.

A D Pogrebnjak Sumy State University,
ul. Rimskogo-Korsakova 2, 40007 Sumy, Ukraine,
Sumy Institute for Surface Modification,
ul. Romenskaya 87, 40030 Sumy, Ukraine
E-mail: alexp@ekt.sumdu.edu.ua, alexp@i.ua
A G Ponomarev Sumy State University,
ul. Rimskogo-Korsakova 2, 40007 Sumy, Ukraine
A P Shpak, Yu A Kunitskii Kurdyumov Institute for Metal Physics,
National Academy of Sciences of Ukraine,
bulvar Akademika Vernadskogo 36, 03680 Kiev-142, Ukraine

Received 8 February 2011, revised 14 April 2011
Uspekhi Fizicheskikh Nauk **182** (3) 287 – 321 (2012)
DOI: 10.3367/UFNr.0182.201203d.0287
Translated by Yu V Morozov; edited by A Radzig

1. Introduction

Leading experts predict a breakthrough in the use of nanomaterials and nanotechnologies in aviation, space research, the chemical, engineering, and motor industries, medicine, biology, and environmental science by the mid-21st century. It poses the questions of diagnosing properties of nanomaterials and nanoobjects and prognostication of their properties under various conditions of application. Two routes of development of analytic techniques are conceivable:

(1) Elaboration of new methods for the rapid acquisition of information at the atomic and subatomic levels.

(2) Reconstruction (or extension) of the potential of the existing methods recognized as efficacious tools for obtaining microlevel information.

Traditional methods for analysis at the substructural (nano-) level, such as high-resolution transmission electron microscopy (HRTEM) and atomic force, scanning tunneling,

and magnetic microscopies, are currently insufficient to seek comprehensive subatomic information about a nanoobject. Hence, the necessity of extending the functional potential and sensitivity of the existing methods for nuclear–physical analysis, including — first and foremost — the analysis of angstrom-sized nanoobjects (e.g. at the level of a cell or in a single-ion acceleration mode). Therefore, the use of nuclear micro- and nanoprobes, as well as pulsed scanning and transmission positron microscopes and microwave microscopes, may help to obtain reliable information on nanoobjects, nano-sized particles and cells to enable researchers to deliberately modify the properties of nanomaterials, nanoobjects, nanoparticles, and nanosystems.

Investigations into the various properties of materials and objects at the micro- and nanolevels, as well as their diagnostics, opening opportunities for the creation of such small-sized structures, are among the top priority areas for modern science and technology. Realization of these opportunities implies the development of new multiinstrument facilities (MIFs) and methods on which to base the analysis of the microstructure and elemental composition of novel nanomaterials and nanoobjects, as well as technologies for their fabrication. The focusing of charged particle beams appears to be of special interest among a variety of underlying physical principles behind the development of new MIFs due to the fact that the minimum size of a currently attainable focused beam lies in the nanometer and subnanometer ranges. Owing to this, the detection of the products of interaction between beam particles and matter provides information on the microstructure and elemental composition of the test objects or allows one to locally modify their physical and chemical properties at the nanoscale level and to further treat the irradiated regions for the creation of small-sized structures.

Multiinstrument facilities built around focused electron beams are materialized in scanning electron microscopes (SEMs) and scanning transmission electron microscopes (STEMs), as well as in MIFs for electron probe lithography (EPL). The processes of beam generation in axisymmetric systems of these MIF are known fairly well. Various types of multipole aberration correctors and energy filters are needed to improve MIFs characteristics. These MIFs find application in electron probe microanalysis (EPMA) of the structure and elemental composition of samples under study, including energy dispersive spectroscopy (EDS) and wavelength dispersive spectroscopy (WDS) [1], Auger electron spectroscopy [2], electron energy loss spectroscopy (EELS) [3], and Z-contrast imaging [4]. Despite the very high (atomic-level) resolution of some of these methods, the peculiar properties of electron beams impose important physical limitations on their application. Strong scattering of an electron beam on the electrons of atomic structures in the subjects being studied necessitates the use of thin samples to maintain high spatial resolution and sensitivity; it puts into question the representativeness of the data obtained with such samples for real materials. Characteristic X-ray emission induced by an electron beam and recorded by EDS or WDS is associated with a high bremsstrahlung background that impairs the sensitivity of microanalysis. The creation of nonprismatic small-sized 3D structures by the EPL method also encounters difficulties caused by electron scattering in high-resistance materials, the formation of high-energy secondary electrons, and an additional radiation dose at the edges of the passed beam.

Focused beams of low-energy heavy ions are utilized in MIFs for secondary-ion mass spectrometry (SIMS). The beams are generated with the help of axisymmetric electrostatic optics, the characteristic mechanism of beam–matter interaction being the scattering of incident ions from atomic nuclei of the sample [5, 6]. Rearrangement of atoms in the near-surface layer under the effect of beam ion momentum transfer results in chemical and structural changes, such as the dispersion of atomic, molecular, and cluster structures. By way of example, the dispersion rate for a Ga-ion beam with an energy of 30 keV varies from 1 to 10 target atoms per incident ion, depending on the type of material. Notwithstanding the high spatial resolution and sensitivity of the method, it is destructive and semiquantitative.

These brief introductory notes allow concluding that the majority of microanalytic techniques are suitable for investigations into the local properties of the surface layers of nanomaterials, nanosystems, and nanoobjects or specially prepared thin samples, which determines the 2D geometry of the region of interest. EPMA is most commonly employed to study bulky 3D specimens, as having a detection limit of about 100 ppm and spatial resolution of ≈ 1 μm predetermined by the physical mechanisms of focused beam electron passage through the material. For this reason, the present review is concerned with methods using other types of charged particle beams and microwave radiation that permit increasing both spatial resolution and sensitivity of analysis of small-sized 3D nanomaterials, nanosystems, and nanoobjects.

2. Scanning nuclear microprobe

The scanning nuclear microprobe (SNMP) is a relatively new MIF designed for studying the structure and elemental composition of samples and direct proton beam writing (PBW) [7, 8]. Used in this MIF is a focused beam of light (hydrogen and helium) ions with an energy of several megaelectron-volts. Such a beam passing through a test subject undergoes only slight expansion in its transverse dimension and penetrates as deep as a few dozen micrometers, with bremsstrahlung background being very low. Due to this, the spatial resolution of SNMP depends on the probe size at the sample surface, while the sensitivity of the microanalysis of certain nuclear–physical methods is at the level of 1 ppm. It makes possible investigations of near-surface layers of thick samples without detriment to spatial resolution and sensitivity. During its 40-year history, SNMP has been widely applied in such different fields as materials science [9–11], microelectronics [12], geology [13], botany [14], biophysics and medicine [15–17], archeology and the arts [18], the environmental sciences [19, 20], microimplantation [21, 22], and the manufacturing technology of 3D micro- and nano-sized structures [23, 24].

In order to better illustrate the peculiarities and the potential of SNMP, it is worth considering the processes associated with the passage of high-energy (MeV) ions through matter.

2.1 Physical mechanisms of interaction between high-energy light ions and solid-state matter

Light ions with an energy of several megaelectron-volts are known to interact with both atomic electrons and nuclei of sample material. However, the probability of ion–electron interaction at the first half of the ion path is a few orders of

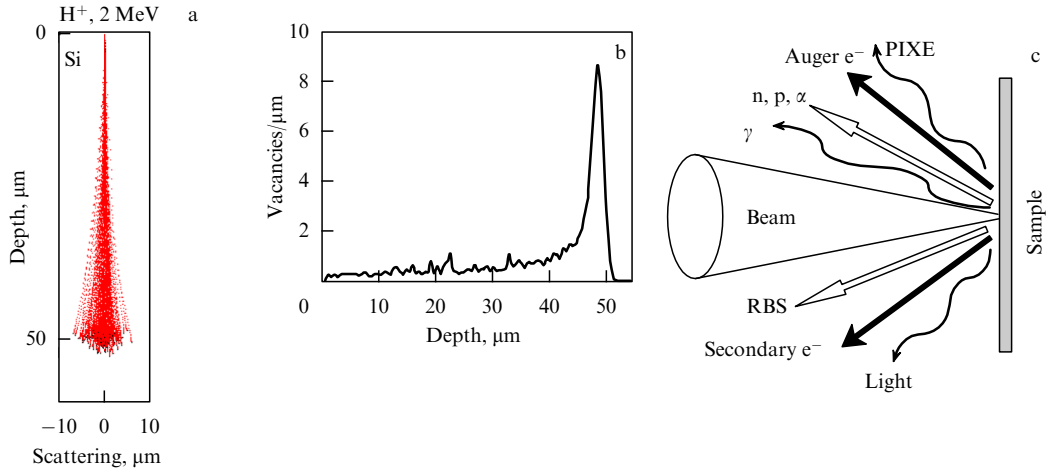

Figure 1. Characteristics of 2-MeV H^+ ion passage through bulk Si: (a) ion paths, (b) generation of vacancies per unit vertical length [27], and (c) secondary products of beam ion–sample interplay.

magnitude larger than that of scattering by atomic nuclei [25]. Due to the great mass difference between interacting ions and electrons, their interplay does not significantly change the incident ion trajectory, which is virtually a straight line (Fig. 1a). The energy lost by the ion in such collisions being small (to conserve momentum), thousands of interactions with atomic electrons may occur before the ion loses all its kinetic energy. The steady loss of energy by a moving ion accounts for the practically uniform depth distribution of the introduced dose. As the ion loses energy, and therefore slows down, the probability of its interaction with atomic nuclei increases and the trajectory appreciably bends, causing the ion to follow a curved path (Fig. 1a). A distinctive feature of mid-energy light ion beams compared with electron beams is the practically total absence of secondary electrons with an energy that could markedly affect the material fluence (proximity effect). The ion penetration depth in a given material depends on the ion energy and is strictly determined; this important property permits creating 3D multilevel objects in high-resistance monolayer materials. Calculations using the SRIM numerical code [26] indicate that protons with an energy of 2 MeV traveling in silicon penetrate as deep as ≈ 50 μm and are deflected from the axis within about 3 μm at the end of their path.

Traveling beam ions with a sufficiently high energy can displace atoms in the Si crystal lattice and thereby alter the local electric properties along their trajectories. Figure 1b shows that the ions lose most of their energy at the end of their path and create a large number of vacancies. Such defects in the Si bulk can be used in two ways. First, to create small-sized 3D structures during irradiation of a definite region by a focused beam of light ions with MeV energies and a fluence sufficient to produce porous silicon by electrochemical etching only in the nonirradiated region. After the completion of etching, the sample is placed in a KOH solution where the porous silicon is removed and only the irradiated region remains. See paper [27] for a more detailed description of this process. The other way of using the irradiated Si region has its origin in the formation of a deeper region in the last part of the ion path with an increased refractive index due to high vacancy density (Fig. 1b).

Atomic interactions with beam ions result in the formation of some secondary products, besides internal structural changes in bulk specimens of resistive materials; detection of these products provides information on the local elemental composition in the scanned region. Figure 1c demonstrates secondary products, such as particle-induced X-ray emission (PIXE) brought about by beam ions, nuclear reaction products (n, p, γ-, and α-particles), Rutherford backscattering (RBS) ions impinged on atomic nuclei, secondary and Auger electrons, and visible light.

2.2 Physical basis of the scanning nuclear microprobe

A scanning nuclear microprobe represents a combination of several devices and systems based on different physical principles. Their traditional layout is illustrated in Fig. 2. As a rule, a plasma ion source produces a beam accelerated to the necessary energy of a few megaelectron-volts in an electrostatic accelerator. Ions of the desired type are selected by an

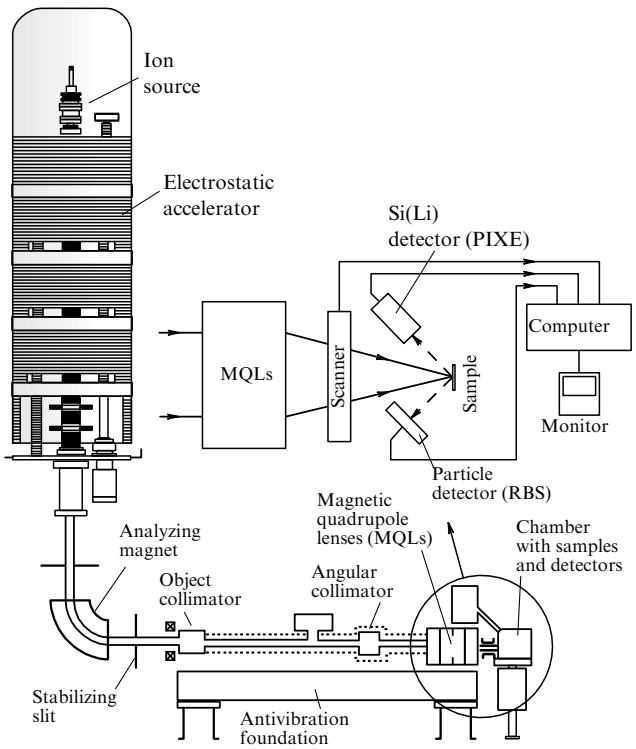

Figure 2. Traditional layout of elements and systems in an SNMP [9].

analyzing magnet having an output slit. The beam formation in SNMP is performed with controling electromagnetic fields, and the system transforming an ion beam into the probe is known as the probe-forming system (PFS). Here, the preliminarily formed beam is transformed into the probe by the object and angular collimators with the help of a focusing system composed of a set of active ion-optical elements, such as quadrupole lenses or a superconducting solenoid. The probe position at the sample surface is altered by the mechanical or electromagnetic systems that displace either the sample or the probe, respectively.

This traditional SNMP setup is a product of historical developments. Ion beam microanalysis became one of the applications of electrostatic accelerators after the main nuclear constants had been determined with the help of these facilities, and the physics of charged particle beams had centered on high-energy ranges. Local irradiation of biological objects with the analysis of nuclear reactions required focusing MeV-energy light ion beams for increasing beam density with the aim to reduce the irradiated area; hence, the name 'nuclear microprobe'. In fact, it was originally just an attachment now referred to as a channel of an electrostatic accelerator. The early history of SNMP developments is described by one of the patriarchs of the field, G J F Legge [28].

Comparison with such MIFs as a high-voltage electron microscope leads to the conclusion that the electrostatic accelerator with an ion source and the analyzing magnet of SNMP function in the aggregate as a high-voltage ion gun. The major requirement for the improvement of both ion and electron guns is the enhancement of brightness and current stability of the beam coupled to the reduction of energy spread of the charged particles. Probe-forming systems must show high acceptance scaled to the probe size directly related to the high reduction factor D (or scale factor, a characteristic similar to that of optical microscopes) at low aberrations. These requirements govern trends in the development of beam formation methods in SNMP, which are based on the traditional layout of its constituent elements. The main factors determining spatial resolution of a microprobe (minimal probe size at a given current strength) include:

- brightness of the ion source;
- energy spread of the beam particles at the exit from the accelerator;
- quality of PFS elements;
- choice of optimal PFS parameters;
- effect of external parasitic electromagnetic fields;
- magnitudes of vacuum pressure, vibrations, etc.

2.3 High-voltage ion gun of the scanning nuclear microprobe

Today, charged particle beams are accelerated by a variety of methods designed to build up an accelerating voltage. The main problem is to ensure that a charged particle accelerator produces a high-brightness beam of the desired energy with its small spread; otherwise, chromatic aberrations of the focusing elements will not allow creating a probe of the required size.

Electrostatic accelerators are classified in terms of the type of conductor — the charging unit of the high-voltage terminal. Van de Graaf accelerators have a conveyer belt to transport charges [29]. The rubber or synthetic belt carries a positive charge toward the high-voltage terminal where the belt is discharged. A disadvantage of such a mechanism is that it is difficult to dynamically control discharging, which leads to temporal instability of the conductor potential and restricts, in turn, the energy spread of the particles in the beam at the level of $\Delta E/E \sim 10^{-3}$. Current instability lies in the range of $\pm 10-30\%$ [30, 31] and does not appreciably change the resolving power. However, this parameter is of importance in charge normalization for quantitative analysis and obtaining a contrast image of the sample surface with secondary electrons. The nonuniform brightness of the image in this case is attributable to the impossibility of accurately controling the charge coming with beam ions.

The accelerators of the National Electrostatic Corporation (NEC), USA have an inductive type Peletron charging unit with the energy spread improved up to $\Delta E/E \sim 10^{-4}$ [32, 33]. One of the main drawbacks of both accelerator models is the mechanical charge transport fraught with vibrations, which hamper the achievement of high resolution in a nuclear microprobe.

Currently, Cockroft–Walton type accelerators with a specific high-voltage terminal [34] are considered to be the most promising for microprobe applications. This approach is based on using electronic high-voltage-multiplication circuits containing no mechanical parts, and are therefore free of vibrations. To date, the highly stable Singletron electrostatic accelerator has been developed by High Voltage Engineering Europe (HVEE), the Netherlands with a maximum conductor voltage of 3.5 MeV [35], which ensures an energy spread of the beam particles up to $\Delta E/E \sim 10^{-5}$ and practically eliminates chromatic aberrations.

A major characteristic of an ion source in accelerators is its brightness, defined as current density per unit solid angle. The total current at the surface of a sample or a target is the product of paraxial brightness of the ion beam and its transverse phase volume that the probe-forming system is able to transport into the target plane with a minimal spot size. Therefore, the ion sources with highest brightness are utilized to obtain the highest beam current at a maximally attainable transverse phase volume in accelerators with a scanning nuclear microprobe channel. High-frequency (HF) sources have found wide application in electrostatic accelerators. The search for new physical principles and technologies called to modernize HF sources with a view of increasing the brightness of HF sources is currently underway. For example, the standard HF source installed at the Institute of Applied Physics (IAP) of the National Academy of Sciences of Ukraine (NASU) was modified by mounting a system of annular permanent Sa–Co magnets creating such a magnetic field configuration that increases the source brightness by a factor of three or more, up to 10 pA μm^{-2} $mrad^{-2}$ MeV^{-1}. The employment of a special configuration of the magnetic field and optimization of the beam extraction and transport system permitted enhancing the paraxial brightness of the HF source by a factor of more than ten [36–38]. However, these data indicate that electron guns afford brightness exceeding that of the available HF sources at least by two orders of magnitude.

Essentially different ion sources for SNMPs, besides HF ones, were also considered with a view to radically increase the ion beam brightness up to that of electron sources. Liquid-metal ion sources (LMISs) with the brightness on the order of 10^6 pA μm^{-2} $mrad^{-2}$ MeV^{-1} proved inapplicable for certain microanalytic techniques that require a significant rise in the ion beam energy to ensure similar conditions of interaction between hydrogen and helium ions and the atoms

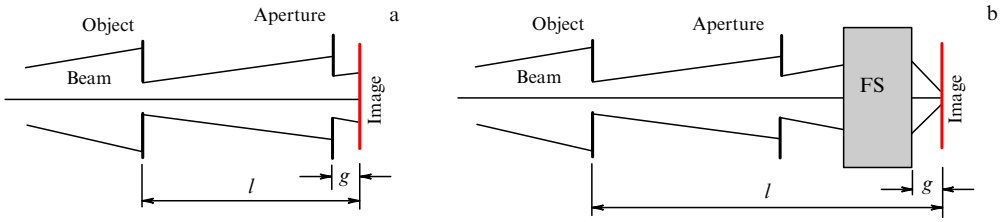

Figure 3. Schematics of PFSs: (a) passive, and (b) active, with the use of a focusing system (FS); l — system length, and g — working distance.

of the sample material. The application of LMISs with Ga^+ ions for creating a microprobe with a beam energy of 500 keV to modify materials for microelectronics was considered in paper [39]. However, the low current of such a source and the large divergence angle of the primary beam impose strong aberration constraints on the entire optical system of the device. The failure to obviate them prevented a substantial improvement in resolution.

Results of numerous studies of gas field ion sources (GFISs) with a fantastic brightness of 10^9 pA μm^{-2} mrad^{-2} MeV^{-1} [40, 41] indicate that their straightforward application in SNMP encounters difficulties arising from certain technical constraints (temperature < 77 K, and pressure $\leqslant 10^{-10}$ Torr). It is practically impossible to create such conditions in the high-voltage part of an electrostatic accelerator under a conductor placed in an insulating gas medium at high pressure. The general requirements for high-brightness sources to be used in electrostatic accelerators for SNMPs are expounded in Refs [42, 43]. The authors emphasized the necessity of the most thorough analysis of ion beam-forming optics, bearing in mind that large divergence angles in these sources may enhance the effect of spherical aberrations on the beam transport conditions in the accelerating tract and the primary beam formation at the entrance to the PFS.

Also worthy of note is the employment of cyclotrons as the accelerators for an SNMP ion gun. The first application of a cyclotron for this purpose was demonstrated in Amsterdam in 1979 [44], despite the low brightness of the beam generated in the ion sources based on electron-cyclotron resonance. Currently, the most successful cyclotron in operation, the JAEA AVF in Takasaki, Japan, utilizes heavy (mostly single) ions for research in biology and microelectronics. The upgrade of the cyclotron allowed achieving an energy resolution of 0.02% for 90-MeV protons, and 260-MeV $^{20}Ne^{+7}$ ions [45, 46].

2.4 Probe-forming systems of the scanning nuclear microprobe

Probe-forming systems of charged particle beams are concentrating ion-optical systems unintended for obtaining correct images of the object of interest. The main requirement for the PFS is an adequately sized probe with a beam current sufficient for experimental studies. The goal of minimizing the probe size that determines resolving power is in conflict with that of maximizing the probe beam current directly related to the sensitivity of the microanalytic techniques being used. Indeed, the probe can be made smaller by decreasing the beam current, while an increase in the current results in a greater probe size.

The PFS can be categorized into passive and active based on the methods of beam formation. The simplest and most primitive PFS scheme comprises two diaphragms that collimate the beam (Fig. 3a). The first diaphragm is called the object collimator, since its aperture sets the object size. The second diaphragm limits the angles of beam divergence and is referred to, in analogy with light optics, as the aperture or angular collimator. Such collimator systems were the first passive PFSs of SNMPs used for microanalysis based on resonance nuclear reaction method [47, 48], with a probe size of ~ 100 μm.

Current density in the probe is naturally increased by utilizing active ion-optical elements focusing the beam (Fig. 3b). In such a setup, the probe-forming system of a nuclear microprobe consists of object and angular collimators forming the initial phase space of the beam and a set of lenses making up the focusing system (FS). The probe-forming process includes transformation of beam particle phase coordinates from the plane of the object collimator into that of the sample image in accordance with the approximate solution of the nonlinear differential trajectory equations describing beam dynamics in electric and/or magnetic fields of different symmetry types. In the aberration theory for charged particle optics, this solution has the form

$$x_t \approx \frac{x_{ob}}{D_x} + \left\langle \frac{x}{x'\delta} \right\rangle x'_{ob}\delta + \sum_{\substack{i,j \\ 2 \leqslant i+j \leqslant 3}} \left\langle \frac{x}{x'^i y'^j} \right\rangle x'^i_{ob}\, y'^j_{ob}\,,$$

$$y_t \approx \frac{y_{ob}}{D_y} + \left\langle \frac{y}{y'\delta} \right\rangle y'_{ob}\delta + \sum_{\substack{i,j \\ 2 \leqslant i+j \leqslant 3}} \left\langle \frac{y}{x'^i y'^j} \right\rangle x'^i_{ob}\, y'^j_{ob}\,, \qquad (1)$$

where $(x_{ob}, y_{ob}, x'_{ob}, y'_{ob})$ are the phase coordinates of beam particles in the plane of the object collimator; (x_t, y_t) are the coordinates of particle deflection from the axis in the sample (target) plane; δ is the momentum spread of the particles; $D_{x(y)}$ are the PFS reduction factors; $\langle x/x'\delta \rangle$, $\langle y/y'\delta \rangle$ are chromatic aberrations, and $\langle x/x'^i y'^j \rangle$, $\langle y/x'^i y'^j \rangle$ are intrinsic and parasitic spherical aberrations of the PFS, respectively.

Relation (1) holds for stigmatic beam focusing and in the case when the contribution of other geometric and parasitic aberrations is smaller compared with chromatic, intrinsic, and parasitic spherical aberrations like those in PFSs of SNMPs. It follows from (1) that PFSs with large D are capable of ensuring small probe sizes with a sufficiently large object collimator. However, high-D systems have greater aberrations, which necessitates reducing the size of the angular collimator. This discrepancy peculiar to PFSs of SNMPs requires seeking solutions to increase reduction factors without a significant increase in aberrations. Therefore, there is a variety of active PFSs in which probes are formed using various combinations of active elements to modulate the ion-optical properties of PFSs and influence the resolving power of SNMPs.

2.4.1 Probe-forming system with a superconducting solenoid. A comparative analysis of the focusing properties of magnetic axially symmetric lenses used in SEMs revealed limitations on their application for light ion beams with an energy of several megaelectron-volts [8]. The estimation was made based on the value of magnetic induction, $B^2 \sim mT/q^2$, necessary to focus a charged particle beam with energy T, mass m, and charge q. In order to reach parameters of the same order of magnitude as electron probe characteristics when using a proton beam with an energy of 1 MeV, magnetic induction must be an order of magnitude greater than the saturation limit (~ 2.5 T), even for special magnetic materials. Insufficient value of the magnetic induction does not allow the working length g to be smaller than 20 cm for solenoids containing no superconducting elements; it restricts, in turn, the reduction factor to about 10 [49].

The employment of superconducting solenoids somewhat improves the characteristics of axially symmetric ion-optical elements for PFSs of SNMPs. Today, a superconducting solenoid is used as the active focusing element of SNMP in Bochum, Germany [50, 51]. The resolving power of this unit is 0.6×0.7 μm with the proton beam current $I \approx 100$ pA and the ion energy 3 MeV. The length of the PFS measures about 6 m, maximum reduction factor $D = 80$ at the minimal working distance $g = 7.5$ cm and the maximum magnetic induction $B = 8$ T. A tandem electrostatic accelerator with a Dynamitron type charging unit (maximum voltage 4 MV, proton beam brightness $b = 1.5$ pA μm^{-2} mrad^{-2} MeV^{-1}, energy spread of the beam particles $\Delta E/E = 5 \times 10^{-4}$) serves here as the ion gun. Nonetheless, despite the sufficient parameters of SNMP, superconducting solenoid-based PFSs have limited application for some analytic techniques due to large scattered magnetic fields.

2.4.2 Multiplets of quadrupole lenses. Quadrupole lenses represent one more type of ion-optical elements for beam formation in SNMPs that are attracting the attention of physicists. Such lenses ensure strong focusing because the focusing field is normal to the beam axis, in contrast to axially symmetric lenses in which only the tangential field component contributes to the focusing. The optical power of electrostatic and magnetic quadrupole lenses is due to dimensionless excitation of pole tips κ_E and κ_M, respectively. The optical power of a magnetic quadrupole lens (MQL) depends on the geometric and physical characteristics of both the lens and the beam, whereas that of an electrostatic quadrupole depends only on the same parameters of the lens:

$$\kappa_M = L_{eff}\left(\frac{q}{\sqrt{2mT}}\frac{B_p}{r_a}\right)^{1/2}, \quad (2)$$

$$\kappa_E = \frac{L_{eff}}{r_a}\left(\frac{V_p}{V}\right)^{1/2}, \quad (3)$$

where L_{eff} is the effective length of the lens field; q, m, T, V are the particle charge, mass, and energy and the potential difference passed by the beam particles, respectively; B_p is the magnetic induction at a pole of the magnetic quadrupole; V_p is the pole potential of an electrostatic quadrupole, and r_a is the lens aperture radius.

A distinctive feature of quadrupole lenses is focusing in one transverse direction and defocusing in the other one. Therefore, a system of lenses is needed to ensure focusing in both directions. By the late 1960s, quadrupoles were applied in high-energy beam transport systems where higher-order aberration effects were negligibly small. Therefore, their use in PFSs was a novelty and there were concerns that aberrations and technical complexities would hamper probe formation with the desired characteristics. In the same period, theoretical studies of the systems of quadrupole lenses were carried out in the framework of the development of high-voltage electron microscopes [52, 53]. Soviet scientists proposed employing a system of four quadrupole lenses with two independent power supplies [54, 55]. It was shown in this work that such a system with the quadrupoles connected antisymmetrically to power supplies is analogous to an axially symmetric lens due to the equality of reduction factors in both transverse directions. In later publications, this system of quadrupole lenses became known by the name 'Russian quadruplet'. It served as a PFS for the first SNMP of the Harwell Research Centre, UK, constructed by J A Cookson and coworkers in the late 1960s [56]. The authors used an MQL with an aperture diameter of 76 mm that had been previously employed in the beam transport system (the resolution achieved was 15×15 μm at a current of ~ 15 nA). Still later, special lenses with an aperture diameter of 38 mm were manufactured, and a resolution of 4×4 μm was reached at a current density of 30 pA μm^{-2}. Thus, great progress was made in comparison with PFSs based on the beam collimation principle.

The successful creation of the first SNMP exceeded all expectations and gave impetus to the development of similar facilities in many laboratories worldwide with the employment of various types of MQL multiplets (one-, three-, and four-lens systems with different power supplies). One such nuclear microprobe based on the Russian quadruplet of the MQL was designed and constructed in the city of Tomsk, Soviet Union [57]. Later on, a nuclear microprobe with an MQL doublet was commissioned at the Kharkov Physical-Technical Institute [58] and a 3.0×5.0-μm proton beam was obtained at the target with a 4-nA current and an energy of 2.4 MeV. The common drawback of both facilities is the impossibility of electromagnetic scanning and the absence of a synchronized data acquisition system, which essentially restricts their capabilities. In CIS countries, the first SNMP was created at the NASU Institute of Applied Physics, Sumy. When operated in the microanalysis mode, it has a resolution of 2 μm and a beam current ≈ 100 pA [59, 60]. The PFS of this microprobe constitutes an optimized, distributed Russian quadruplet with two integrated MQL doublets of an essentially new design [61]. The creation of this SNMP was preceded by a series of theoretical studies on the optimization of nonlinear beam-forming processes in quadrupole-based PFSs [62, 63] that revealed the dependence of beam characteristics at the sample surface on the number of lenses and their positioning geometry.

The doublet of quadrupole lenses is the simplest system of this type among various PFSs. The lenses, located as close to the sample surface as possible, are fed by different power supplies and show alternating focusing–defocusing properties in each transverse direction (x, y). Special mention should be made of the recent work [64] describing the upgrade of PFS elements for the SNMP that allowed achieving a resolution of 0.4×0.4 μm at a proton beam current of ~ 10 pA with an energy of 3 MeV. This resolution was estimated by linear scanning over the edge of the standard calibration grid in the x- and y-directions, and analyzing the secondary electron yield. The PFS based on the doublet of a precision MQL

has the following parameters: total length of the system $l = 6$ m, working distance $g = 26$ cm, reduction factors $D_x \times D_y = -35 \times -9$, brightness of the output beam as it leaves the Dynamitron electrostatic accelerator $b = 10$ pA μm^{-2} mrad^{-2} MeV^{-1} with a maximum voltage of 4.5 MV, and the energy spread of the beam particles $\Delta E/E = 6 \times 10^{-4}$.

The study of multiplet configurations of two to four MQLs [65] revealed that triplets of magnetic quadrupoles with highly excited poles have certain advantages over other systems with compact positioning of the lenses. Such a system permits increasing reduction factors with a decreasing of working distance in both the *x*- and *y*-directions without a substantial change in their ratio.

Taken together, these modifications resulted in the highest SNMP resolution to date based on such a PFS known as the 'Oxford type triplet' in a microanalysis mode [66]: probe size of 0.29×0.45 μm at an H^+ beam current of around 50 pA. These data were obtained by linear scanning of the edge of the standard calibration grid in the *x*- and *y*-directions, and analyzing the yield of characteristic X-ray emission. The PFS of SNMP at the Center of Ion Beam Application (CIBA), Singapore University, has the following parameters: total length of the system $l \approx 7$ m, working distance $g = 16$ cm, reduction factors $D_x \times D_y = 88 \times -24$, beam brightness at the exit from the Singletron electrostatic accelerator $b = 74$ pA μm^{-2} mrad^{-2} MeV^{-1} with a maximum voltage of 3.5 MV, and the energy spread of the beam particles $\Delta E/E = 10^{-5}$. The spot size of 35×75 nm at a 1-fA H_2^+ current [66] was also obtained at CIBA for a PFS with the following parameters: total length of the system $l \approx 7$ m, working distance $g = 7$ cm, and reduction factors $D_x \times D_y = 228 \times -60$ at the same characteristics of the high-voltage ion gun. The probe parameters result from linear scanning over the edge of the square 1-μm aperture in the *x*- and *y*-directions, and analyzing H_2^+ ion intensity in the scanning transmission ion microscopy mode.

Further progress in the development of SNMPs was expected to be made using parametric MQL multiplets with the number of lenses and geometry of their location as parameters. This implied theoretical research on PFSs based on four-quadrupole systems fed by Russian quadruplet type power supplies with the first two lenses positioned freely along the optical path. As shown in Ref. [67], the first and the second lenses must be coupled into a doublet and moved in search for the optimal position. The results of Refs [68–70] gave reason for optimism, since the studied systems of the distributed Russian quadruplet permitted considerably increasing both reduction factors and system's acceptance. Major approaches to overcoming the resolution limit of 1 μm in the microanalysis mode are considered in Ref. [71] emphasizing a number of positive factors related to the presence of additional parameters influencing ion-optical properties and possibly improving resolution of the PFS based on distributed MQL multiplets. A distinctive feature of the distributed Russian quadruplet is the isolated location of the first two lenses. The highest resolution in a PFS of this type was obtained for a probe size of 0.34 μm at a proton beam current of around 10 pA [72] by the linear scanning of the edge of the standard calibration grid in the *x*- and *y*-directions. The PFS of an SNMP (LIPSION, Leipzig, Germany) with which these results were achieved has the following parameters: total length $l \approx 9$ m, working distance $g = 30$ cm, reduction factors $D_x \times D_y = 82 \times 82$, beam brightness $b = 20$ pA μm^{-2} mrad^{-2} MeV^{-1} at the exit from the Singletron electrostatic accelerator with a maximum voltage of 3.5 MV, and the energy spread of the beam particles $\Delta E/E = 10^{-5}$.

Studies of distributed PFSs based on the Russian quadruplet and their successful realization in experimental setups gave an impetus to the search for ways to improve SNMPs. One of the ways was the introduction of accessory lenses. As mentioned earlier, an important characteristic of SNMPs, besides the resolving power depending on the spot size at the target, is the strength of the beam current concentrated in the probe. This parameter determines sensitivity of microanalysis, all other detection conditions being equal.

The aim of the work reported in Ref. [73] was to create a high-acceptance PFS operating at a beam current from 0.1 to 20 nA with a resolution of 1–3 μm, i.e. allowing a radical increase in the current, while only slightly enlarging the probe size. This circumstance is of importance for the detection of impurities in samples at a relative concentration of 0.1 ppm that does not yet cause radiation damage of materials or radiation-induced diffusion of microelements. A five-lens PFS was designed to accomplish the assigned task [74]. The total length of the system, $l = 4.7$ m, was limited by the floor space needed to install the SNMP. Special MQLs were developed to ensure the minimal working distance $g = 8$ cm. The following experimental values were obtained: probe size $d = 1.3$ μm at a proton beam current $I \sim 0.5$ nA; $d = 1.8$ μm, $I = 8$ nA; $d = 2$ μm, $I = 10$ nA; $d = 3$ μm, $I = 20-25$ nA. A PFS for SNMP (CSIRO-GEMOC, Sydney, Australia) had the following parameters: reduction factors $D_x \times D_y = -65 \times 69$, and beam brightness at the output of the tandem electrostatic accelerator $b = 1$ pA μm^{-2} mrad^{-2} MeV^{-1}.

2.4.3 Focusing elements. The physical principles underlying most focusing elements (FEs) include creation of an axisymmetric external electromagnetic field. This means that a particle traveling along the axis is unaffected by the field, and therefore does not change its direction at the exit from the FE. There are two types of axial symmetry, axial and quadrupole, realized in SNMP focusing elements. Results of theoretical and experimental studies of various FEs with these types of a field symmetry are reported in monograph [65], where some 'exotic' FEs are considered among others, such as plasma and coaxial lenses. However, magnetic axially symmetric lenses based on superconducting solenoids and systems of magnetic and electrostatic quadrupole lenses are used most commonly, because they ensure the highest resolution at the current stage of SNMP development.

Peculiarities of the application of superconducting solenoids in the capacity of FEs in SNMPs are due to certain properties of an axisymmetric magnetic field. A stigmatic image is produced upon changing a single parameter (current strength in solenoid coils). The adjustment depends on four positioning parameters, viz. transverse displacements (x, y), rotations in the yawing plane ($x0z$), and pitch ($y0z$), whereas the alignment of an MQL triplet requires 16 parameters to be controlled. Spherical aberrations are 5–10 times smaller, and chromatic aberrations are comparable to those in quadrupole PFSs. An important drawback of these lenses is their high operating costs due to liquid-helium cooling and the dependence of improving resolution parameters on the magnetic field induction, which is currently limited by the properties of the superconducting materials.

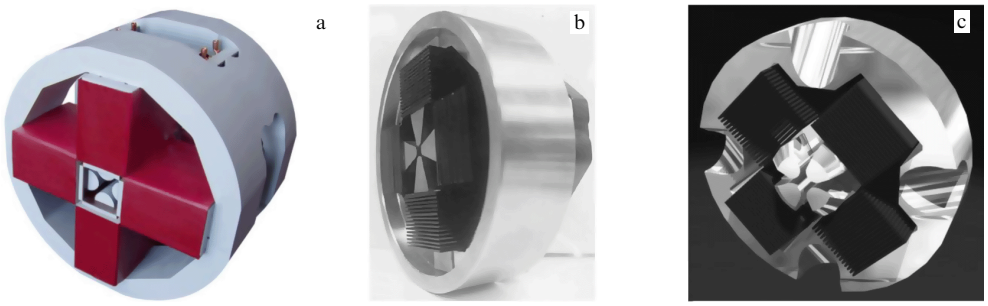

Figure 4. Magnetic quadrupole lenses applied in the beam-focusing systems of nuclear microprobes: (a) integrated doublet (IAP NASU), (b) OM-52 lens (Oxford Microbeam), and (c) CSIRO-GEMOC lens.

FEs with quadrupole field symmetry are most commonly used as active focusing elements in modern SNMPs. Modernization of quadrupoles for the improvement of the resolving power of SNMP facilities dates back to the first successful application of an MQL in the probe-forming system of MeV-energy ion beams. General tendencies in the development of precision quadrupole lenses ensue from the necessity of creating PFSs with a small working distance, because short-focus ion-optical systems have higher reduction factors at moderate aberrations. A reduction of both the working distance and the focal length is associated with an increase in the optical power of quadrupole lenses. It follows from relations (2) and (3) that for fixed beam parameters the optical power of the quadrupoles is directly proportional to the magnetic induction or the pole potential and the effective lens length, and inversely proportional to the lens aperture radius. Despite such a simple dependence, all these parameters have limitations as regards their favorable changes. By way of example, an increase in the effective length is unrelated to the working distance, but leads to a greater focal length. The possibility of increasing magnetic induction depends on both the degree of saturation of a given material and the geometry of the pole tips. Potential growth in an electrostatic quadrupole is limited by vacuum breakdown conditions. A decrease in the aperture necessitates a change in pole geometry that, in turn, causes parasitic multipole field components to grow due to the deviation from the hyperbolic profile and the appearance of local pole saturation zones at the sites of the closest approach of the poles.

An equally important factor is the absence of physical mechanisms for precise mounting of an einzel magnetic quadrupole lens aligned with the beam axis. The transverse lens plane in existing microprobe facilities is placed perpendicular to the laser beam. However, the axis of the light beam does not necessarily coincide with the ion beam axis due to the presence of scattered magnetic fields in the laboratory that cause distortion of the rectilinear beam axis. Therefore, in PFSs with magnetic quadrupoles aligned separately on the optical pathway the lenses need to be coupled into doublets.

The following steps in upgrading magnetic quadrupoles have been taken over the 30-year history of microprobe operation:

- the passage from the cylindrical to hyperbolic shape of pole tips allowed diminishing parasitic higher-order multipole field components;
- the manufacturing technology of nonseparable OM-52 lenses was developed and brought into commercial practice by Oxford Microbeams (http://www.microbeams.co.uk) [75] (Fig. 4b) using electroerosion metal processing with the accuracy of mutual arrangement of pole tips of around 2 μm; this permitted removing parasitic sextupole and octupole field components induced by breaking the quadrupole lens symmetry;
- new designs of magnetic circuits with protruded pole tips (OM-52) and indentations in the magnetic circuit for the placement of ion detectors (CSIRO-GEMOC) [76] (Fig. 4c) were proposed in conjunction with integrated doublets for use in distributed PFSs whose yoke and poles are made from a single piece of magnetically soft material (IAP NASU) [61] (Fig. 4a); these were used to decrease the working distance (from the outer boundary of the effective field of the last lens to the target plane);
- studies on the utilization of magnetic materials with a narrow hysteresis loop for manufacturing magnetic circuits and lens pole tips;
- substantiation of the use of magnetic quadrupoles with superconducting coils to focus $\sim$ 20-MeV ions [77].

3. Local microanalysis with the use of a scanning nuclear microprobe

Methods for local 3D microanalysis of thick samples by application of focused charged particle beams are considered in terms of the requirements for the 'ideal' spatial location of atoms and their identity as chemical elements. The lack of such methods to date dictates the need for estimating the existing microanalytic techniques from the standpoint of their compliance with the 'ideal' requirements. In this context, each method is evaluated by three parameters, viz. spatial resolution, detection limit, and sensitivity. The spatial resolution is determined by the size of the region from which the secondary products of interactions between beam particles and atoms of the sample are released. The detection limit characterizes a minimal content of a certain element detectable with a given reliability; it depends on the possibility of extracting a desired signal from the totality of detected events. The sensitivity of a method is understood as its capability of discriminating between close concentrations of the atoms of a given element. Sensitivity is a function of the cross section of the secondary product yield and the number of particles in the probe. Sensitivity and resolution of most methods are interrelated parameters, because a maintenance of the necessary sensitivity requires a rise in the number of particles or beam current, which, in turn, implies an increase in the probe size. An important characteristic of any method is also the possibility of making the quantitative analysis of the level of elements contained in the region of the sample being studied. The most popular methods for

Table 1. Characteristics of methods for local microanalysis with the use of SNMPs [9, 78].

Method	Resolution, nm	Sensitivity, ppm	Quantitative analysis,%
PIXE	300	< 1	5
RBS	500	10	3
NRA	1000	0.1	3
ERDA	> 1000	500	3
IBIC	< 100	—	none
IBIL	300	—	none
SEE	< 100	—	—

local microanalysis of thick samples with the use of SNMPs are listed in Table 1.

The first four methods collated in this table allow in the aggregate local quantitative microanalysis of all elements.

3.1 Method of characteristic X-ray emission induced by beam ions

The particle-induced X-ray emission (PIXE) method is based on atomic ionization in the sample. The observed X-ray spectrum consists of the continuous spectrum induced by bremsstrahlung radiation of secondary electrons and the linear spectrum produced by recombination of ionized atoms and the filling of K-, L-, and M electron shells. The PIXE method is currently well established; as mentioned above, its advantages are due to the relatively low bremsstrahlung background compared with electron beams in EPMA. Figure 5 represents X-ray spectra obtained for a thick sample using EPMA and PIXE. The comparison shows that the high bremsstrahlung background in EPMA (Fig. 5a) prevents detection of small concentrations of certain elements that are readily identified in the PIXE spectrum (Fig. 5b).

Several software packages for quantitative analysis of PIXE spectra are available. These programs were tested independently under the auspices of the IAEA; the results are published in Ref. [81].

Worthy of special mention is the GeoPIXE software package [81] that allows not only quantitative analysis but also two-dimensional mapping of the location of elements for SNMPs, when the data are acquired during scanning in an event-by-event mode and each event is marked by three parameters, i.e. beam energy and beam positions (x, y) of the PIXE yield. Modification of the PIXE method for the improvement of locality of the analysis implies diminishing the beam spot size on the surface of the object under study. However, it leads to a substantial decrease in the beam current and, therefore, the number of atom ionization events.

The maintenance of the PIXE yield by increasing current density alone when using high-brightness ion sources is somewhat limited by radiation damage to the initial material and defects incorporated into the original sample. Another approach, i.e. increasing the solid angle of the detector by enlarging its area, is inefficient because it lowers detector resolution and enhances the superposition effects of event records within a narrow time interval.

One of the ways to solve this problem is the development of matrix detectors with an appropriate controller for synchronizing a set of all events and improving the sensitivity of the PIXE method up to several hundred ppb. The development of such matrix detectors is discussed in Refs [83, 84]; their controllers govern parallel processes and have the following characteristics: a solid angle of 1.2 sr, energy resolution of ~ 184 eV (Mn Kα), and peak-to-background ratio of $\approx 10^3$. A new parallel data acquisition method permits loading up to 10^8 events per second and practically preventing event overlaps during detection.

The high sensitivity of the PIXE method coupled with submicron spatial resolution of SNMPs is widely used in medical applications, e.g. for the elucidation of factors responsible for a variety of diseases and the analysis of the distribution of chemical elements present at low concentrations in arterial walls [85]. The role of iron in the pathogenesis of Parkinson's disease, the subject of a growing interest among neurochemists, was considered in Ref [86]. It was demonstrated that iron accumulates in abnormally high quantities in the gray matter of Parkinson's patients. The combination of PIXE and scanning transmission ion microscopy (STIM) makes it possible to reconstruct 3D tomograms illustrating the spatial distribution of microelements. Figures 5c, d show a cell of the green algae *Euglena gracilis* for which such a 3D tomogram was obtained.

3.2 Rutherford backscattering and elastic recoil detection

Methods based on the registration of Rutherford backscattering (RBS) energy spectra and recoil nuclei (elastic recoil detection analysis: ERDA) formed in sliding interactions of beam ions with the surface are especially popular for ensuring high accuracy of the analysis of element depth distribution profiles. The depth resolution of the most common semiconducting detectors of charged particles is around 10 nm, compared with ~ 1 Å for detection utilizing specialized spectrometers. In doing so, the samples must have a polished surface. The general physical principles of these methods are expounded in books [88, 89]. Surface roughness remains the main factor hampering the achievement of high-resolution detection for commercial and natural samples and

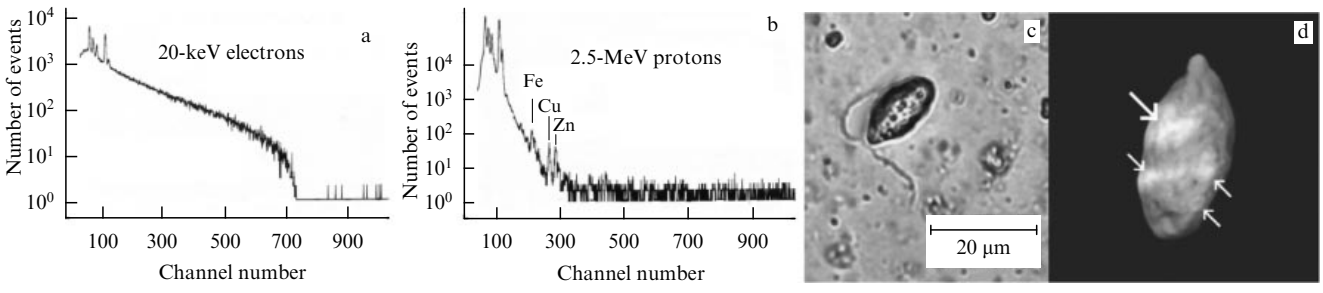

Figure 5. X-ray spectra induced by different types of charged particle beams: (a) electrons, 20 keV, and (b) protons, 2.5 MeV [79, 80]. Optical image (c) and tomogram (d) of green algae *Euglena gracilis*. The surface reconstructed from the STIM data is compared with the high-phosphorus region identified from the results of using the PIXE method [87].

rendering interpretation of experimental data difficult. A new approach to parametrizing Monte Carlo calculations is proposed in Ref. [90]. Numerical codes based on the analytic formulas describing physical processes behind beam particle scattering can be used to rapidly calculate roughness-related effects for a variety of uneven surfaces. Similar to PIXE, RBS spectrometry is supported by several computational programs permitting interpretation of backscattering spectrum profiles. The results of their independent testing are reported in paper [91].

By virtue of its kinematic characteristics, RBS spectrometry is most efficacious for the investigation of the local distribution of heavy elements in light matrices, e.g. for determining heavy metal impurities in biological objects. ERDA is extensively applied to study hydrogen concentration profiles in near-surface layers of various materials [92].

3.3 Nuclear reaction analysis

Nuclear reaction analysis (NRA) or analysis of instantaneous emission accompanying nuclear reactions has its origins in interactions between light ions with an energy of several megaelectron-volts with sample atoms. An ion can overcome the Coulomb barrier of an atomic nucleus and approach as close to it as the nucleus radius; it may induce a nuclear reaction resulting in a structural change of the nucleus. The products of such a reaction are hydrogen and helium ions, neutrons, and γ-radiation recorded with detectors. The energy dependence of the nuclear reaction cross section has a few narrow resonances. Therefore, the probability of a reaction is especially high when beam ions possess an energy of several megaelectron-volts.

As the beam energy grows and reaches a resonant value, nuclear reactions involving one kind of atoms begin to occur on the sample surface. A further rise in the beam energy causes a resonance reaction in deeper layers as a result of ion deceleration, which makes it possible to determine element depth distribution profiles with a resolution of ~ 10 nm and a sensitivity of around 0.1 ppm [93]. Because the Coulomb forces for heavy nuclei markedly decrease the reaction cross section, interactions with the light nuclei of the sample, $Z < 15$, are most efficacious within a beam energy range < 5 MeV. The high selectivity of NRA is due to different energy spectra and cross sections of nuclear reactions for different elements and their isotopes. Experimental facilities for local microanalysis based on the NRA method with the use of SNMPs are described in Ref. [94].

3.4 Registration of ion beam-induced charge

Registration of ion beam-induced charge (IBIC) found a wide application in the 1990s for studies of microelectronic devices, semiconductor radiation detectors, solar cells, distribution of dislocations, etc. This method relies to the full extent on peculiarities of the passage of light ions accelerated to MeV energies in semiconducting materials and insulators. Their small deflections from the straight trajectories ensure high spatial resolution of the method compared with electron beams. The method is based on the formation of electron–hole pairs due to ion energy transfer during the beam passage in a semiconducting material. The possibility of determining the number of newly formed electron–hole pairs is due to a number of internal and external factors, such as recombination at point and extensive defects, impurity concentrations, diffusion length of minority carriers, and electric field strength. The IBIC method utilizes focused light ion beams with an energy of several megaelectron-volts and weak currents (0.1–1 fA). It measures individual charge pulses. Analysis at such low beam currents is possible because each ion generates a sufficiently large number of electron–hole pairs as it passes through a semiconducting material or insulator and the net charge determining the signal amplitude exceeds the noise level of the measuring instrument.

Figure 6 depicts major types of measuring circuits used for registration of IBIC (see review [95] devoted to the general physical principles, the theoretical basis, and application areas of the method in question). It can be seen that charge carriers formed in the depleted region of p–n junctions slowly diffuse from the place of their generation; many of them recombine at point defects, which accounts for a limited number of carriers reaching the contacts of the instrument. The time interval during which a pulse is recorded varies from pico- to microseconds. Under normal measurement conditions, the charge-generated pulse is first accelerated to several volts. Thereafter, the digitized signal marked by the beam position is accumulated in computer memory by the data acquisition system built around the charge-coupled devices (CCDs). The data processing yields information on the sample microstructure in the form of a contrast image of the concentration of electrons and holes [96, 97]. Apart from registration of the total accumulated charge in the case of a fixed beam position, it is just as well possible to measure induced charge evolution time from pulse variations at the contacts (time-resolved IBIC or TRIBIC method). This, in turn, permits estimating the mobility of charge carriers in the sample [98].

3.5 Registration of ion beam-induced luminescence

Registration of MeV ion beam-induced luminescence (IBIL) coupled with PIXE, RBS, or NRA makes it possible to derive information about the chemical nature of various materials. The physical principles behind IBIL are comprehensively described in monograph [9]. The most universal of them is energy transfer from beam ions to valence electrons of atomic structures in a sample, resulting in their excitation.The transition back to the ground state is accompanied by IR, visible, or UV radiation.

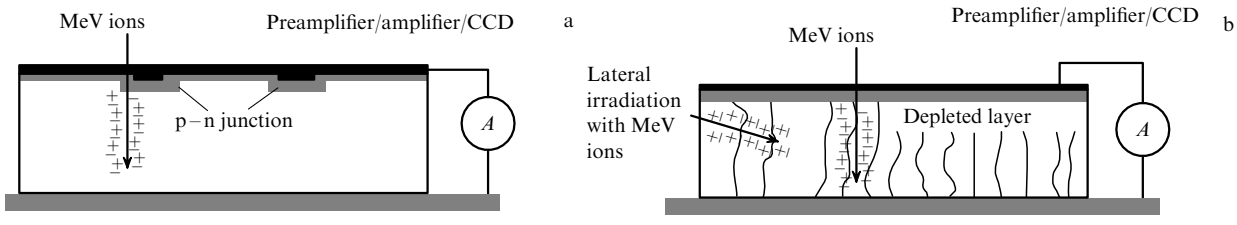

Figure 6. Main variants of composing measuring circuits in the IBIC method: (a) semiconductor device, and (b) semiconductor wafer.

Ion beams with a current of around 100 pA are used to induce luminescence in SNMPs, bearing in mind the low efficiency of detectors accounting for the spatial resolution of the IBIL method on the order of 0.3 μm. In this context, Ref. [99] is worth mentioning, where the upgraded system for registration of radiation in a range of 300–1000 nm was employed and the comparative analysis of photon- and proton-induced luminescence performed. The analysis showed that protons induce more intense luminescence and metastable states. These effects may constitute a basis for a new laser pumping setup. The scope of IBIL applications is rather wide; specifically, the method has been used in biological research at the cellular level [100] and studies of historical artifacts [101] and semiconducting materials [102].

3.6 Single event effects

Methods based on the use of single ions are collectively called single event effects (SEEs). Although such events can be caused not only by ions but also by other types of single impacts on the object being studied (e.g. pulsed electromagnetic radiation or solitary uncharged particles), we shall consider below only individual ions. The most interesting aspect of SEEs is related to the exploitation of civilian and military spacecraft. High-energy particles capable of penetrating deep into microelectronic devices are considered to be the most dangerous form of cosmic radiation. It produces a number of effects responsible for malperformance or complete failure of many devices. A classification scheme of such effects is proposed in Ref. [103].

Among the physical phenomena behind equipment failure is the mechanism of charged particle passage through semiconducting materials [104]. As shown earlier, the loss of energy by ions results in the formation of electron–hole pairs, which accounts for the malfunctioning of a given device, while microstructural defects may cause its complete failure: hence, the importance of radiation resistance of microelectronic instruments and the particular interest in experimental simulation of the related processes.

Miniaturization of microchips and transition to the nanoscale level require the aiming hit of single ions with an energy of tens of microelectron-volts per nucleon exactly in the predetermined region of the sample. The SNMP appears to be the MIF most suitable for such research. However, it should be borne in mind that the spatial resolution in a low-current mode (presently ~ 50 nm) is measured at the half-height of the total beam current distribution over the target and that a large enough halo is present. This fact renders difficult direct application of an SNMP, which led some laboratories to modify microprobe facilities designed to study SEEs with single ions [105–107].

Studies of various microelectronic devices operated in a single-ion irradiation mode with the employment of an SNMP were reviewed in Refs [108, 109]. The authors considered Si–Ge hetero-bipolar transistors (the cross section of one of them is depicted in Fig. 7a). The accumulated charge was measured by scanning with single ions along the horizontal direction. Figure 7b shows the dependence of the accumulated charge on the beam coordinate during irradiation by single ions. Clearly, the charge accumulated at the collector is significantly higher than at the base, and the physical area for the accumulated charge at the collector is much greater than the analogous base area.

Another field of research in the SEE mode currently underway is radiobiology. Unlike microelectronic devices, living cells must be studied under normal (nonvacuum) conditions, maintaining their vital activity. Moreover, the horizontal motion of ions imparts additional complexity to high-precision ion beam guidance. A traditional setup of cell irradiation with single ions is illustrated by Fig. 7c–e.

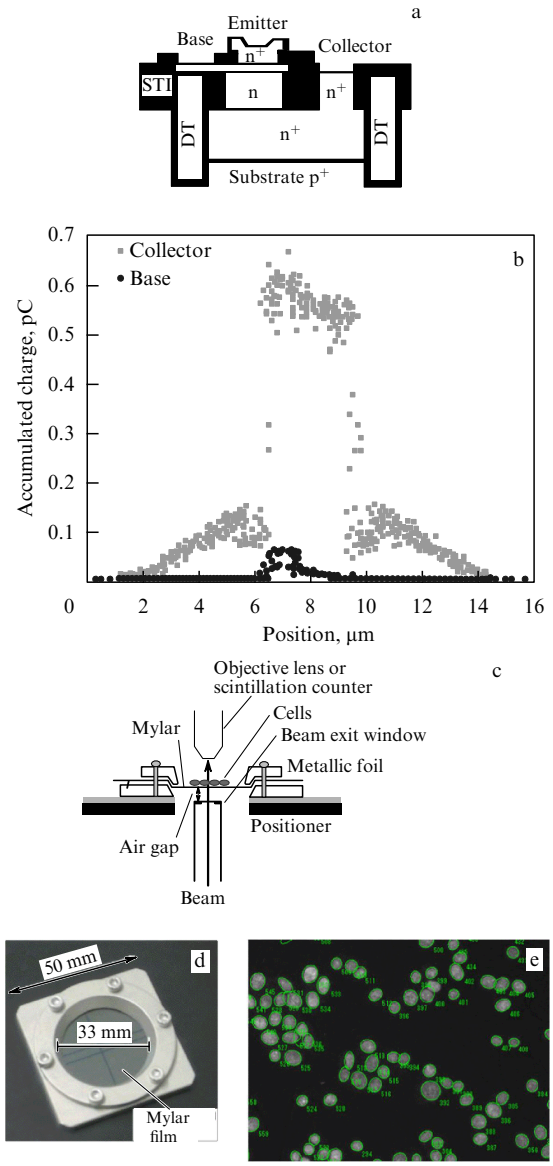

Figure 7. (a) Cross section of Si–Ge hetero-bipolar transistor, (b) charge accumulation at transistor collector and base at different microbeam positions [108, 109]. Traditional setup of single-ion irradiation: (c) schematic layout of the cell dish, (d) mylar dish, and (e) fluorescent cell microimage (each nucleus has a reference number for its identification in a biological experiment) [116].

Of special interest among new, specialized MIFs designed for the study of single-ion irradiation of living cells are those described in papers [110–112]. A unique MIF with a vertically positioned PFS of an SNMP has been constructed in Surrey, UK [113]. This unique multiinstrument facility is intended for the implementation of a cancer cell research project. It is based on a precision tandem electrostatic accelerator and permits *in vitro* irradiation of 100,000 cells per hour, aiming ions at each individual cell with an accuracy of 10 nm. To date, numerous data on the influence of single ions on living cells have been published (see, for example, Refs [114, 115]).

4. Modification of materials for the creation of small-sized 3D structures

The first proton beam writing (PBW) studies were published in the late 1990s [117–119]. They demonstrated the possibility of utilizing focused 2-MeV proton beams to create microcomponents and revealed a number of physical principles making PBW a promising technology for producing nanostructures. In the past decade (2000–2010), this technology was being developed along several lines, including the improvement of focused beam characteristics and the evaluation of beam interactions with a variety of resistive materials. A theoretical analysis of manufacturing sub-100-nanometer structures was undertaken [120]. An important advantage of PBW is the possibility of obtaining nanocomponents with a high aspect ratio (160:1), making such structures essentially three-dimensional. This required evaluation of the influence of different conditions of focused ion beam irradiation on the quality of resultant nanocomponents. In the experiments reported in Refs [121, 122], the roughness height at the side walls was measured to range from 3 to 7 nm depending on the type of the resistive material and the irradiation algorithm. This characteristic is of importance for applications where nanocomponents serve as channels for flowing liquids and for creating nanostamps. Another important characteristic is side wall prismaticity. As shown in paper [123], since the proton trajectories in a resist material are rectilinear, the angle between the side wall and the surface is 89.5°. Further improvement of PBW technology is currently underway in several laboratories [124, 125]. Operating modes and irradiation conditions for various resists are fairly well established. Proton fluences and characteristic dimensions of the resulting small-sized components for different types of resists are listed in Table 2.

Using hydrogen silsesquioxane (HSQ) as a resist, a structure in the form of a separately standing line (a protrusion with a characteristic width of 22 nm) was obtained [127] (Fig. 8). The next step was the introduction of the results of studies into production systems for manufacturing nanocomponents. A PBW-based MIF was developed at the Shibaura Institute of Technology, Tokyo, Japan, for market promotion and industrial application [128].

Micro- and nanostructures produced by focused charged particle beams have a broad range of applications, some of which are discussed below.

Table 2. The use of various resistive materials in PBW technology [126].

High-resistance material	Type of material	The fluence required, nC mm^{-2}	The smallest characteristic size obtained
PMMA	Positive	80 – 150	20 – 30 nm
SU-8	Negative	30	60 nm
HSQ	Negative	30	22 nm
PMGI	Positive	150	1.5 μm
WL-7154	Negative	4	800 nm
TiO_2	Negative	8000	5 μm
Si	Negative	80,000	15 nm (needle point)
DiaPlate	Negative	10	10 μm
ADEPR	Negative	125 – 238	5 μm
Forturan	Positive	1	3 μm
PADC (CR-39)	Positive	600	5 μm
ma-N 440	Negative	200	400 nm
GaAs	Negative	100,000	12 μm

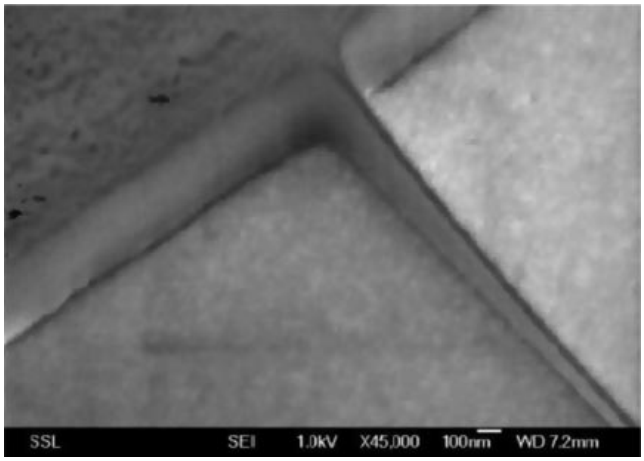

Figure 8. Image of a separately standing line — a protrusion with a high-aspect ratio and a characteristic width of 22 nm — obtained by exposure to focused 2-MeV proton beam [127].

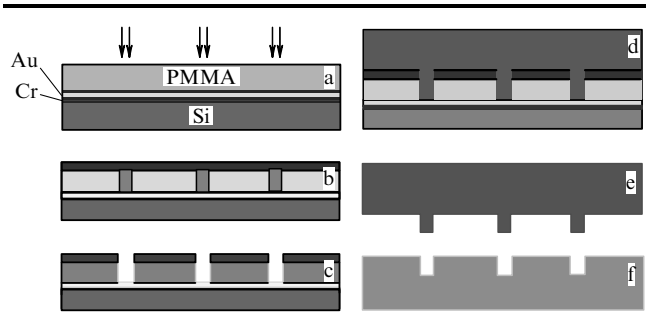

Figure 9. Schematic of nanostamp fabrication by PBW technology [129].

4.1 Nanoimprinting

Projection optical, X-ray, and electron- and ion-beam lithographies are most frequently used for batch production of small-sized structures arranged with high density over a large area. However, the technical complexities and the anticipated increase in the manufacturing costs of producing sub-100-nm structures necessitate the search for alternative solutions. The combination of lithographic technologies using focused charged particle beams with nanoimprinting may be a method of choice for some specific purposes [129, 130]. By way of example, Fig. 9 shows a process flowchart for manufacturing 3D stamps relying on PBW technologies and Ni electrodepositron. The Si(100) substrate is first covered with Cr (20 μm) and Au (200 μm) layers to enhance adhesion and electric conduction, then a layer of polymethyl methacrylate (PMMA) resist is centrifugally deposited and irradiated by a focused proton beam with an energy of 2 MeV (Fig. 9a). Thereafter, another metallic layer is laid on the upper surface to form the stamp base and ensure the conductivity needed for electrodeposition (Fig. 9b). Treatment with a developer results in a three-dimensional structure (Fig. 9c), then a nickel electrodeposition is executed (Fig. 9d). The process is completed by separating the stamp from the template (Fig. 9e) and nanoimprinting (Fig. 9f). Such stamps can be reused up to 15 times in succession without an appreciable deterioration of reproducibility.

4.2 Biophysics and medicine

The narrow channels produced by PBW technology are tens of nanometers wide and their height is a few dozen times greater than the width. They can be employed to study

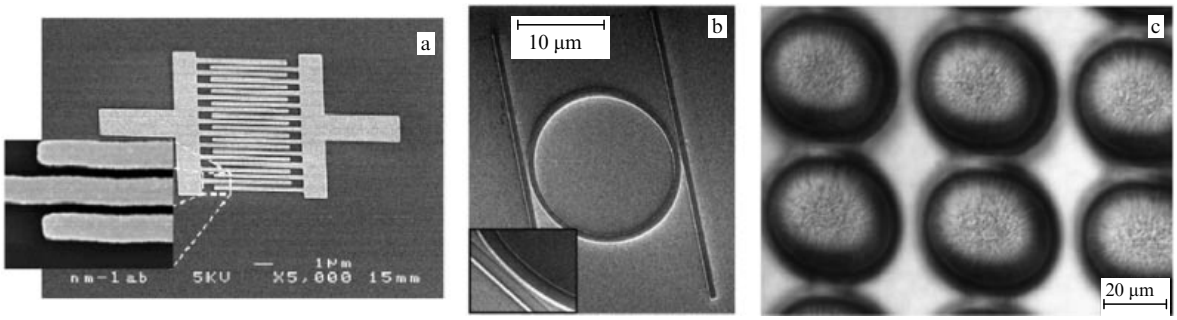

Figure 10. An image of a nanobiosensor structure [131]. (a) Optical components produced by proton beam writing. (b) Images of a ring resonator created in a layer of SU-8 resistive material on an Si substrate; the inset shows a well-defined space with specific features of 200 nm in size [131]. (c) Optical image of a microlens array fabricated from a 15-μm thick PMMA resistive material [131].

biomolecules. Figure 10a depicts a prototype biosensor structure (interdigital electrodes with a gap of ~ 85 nm). Information about biomolecules is derived from the measurement of total electric resistance between the electrodes. Inasmuch as each specific type of biomolecules has a definite electrical conductivity, such a sensor can be applied to study a variety of biomolecules, including simple toxins (e.g. formaldehyde), large DNA sequences, hormones, and more specialized biomolecules, such as anti-HIV antibodies.

4.3 Microphotonics and microoptics

The scope of applications of micro- and nanostructures produced using proton beam writing includes microoptics and microphotonics. Processing light signals is possible with the use of chip-integrated optical elements, such as emitters, waveguides, detectors, modulators, and large arrays of microlenses to ensure high-speed data processing. There are basically two ways in which PBW technology can be applied. The first involves the formation of small-sized structures by the direct patterning of polymers layered by centrifugation over a proper substrate, such as glass or a thermal oxide layer on a silicon wafer. For applications in light guiding, both the substrate and the cladding need to be of a lower refractive index than the core material of the optical fiber. The SU-8 resist appears to be the most suitable material for making waveguides due to its high transparency, low loss of the light signal, and smooth walls (Fig. 10b). Furthermore, the refractive index of SU-8 is only slightly above that of glass substrate materials and thermal silicon oxide.

Microlens arrays can be manufactured utilizing structures composed of a layer of a resistive material laid centrifugally on a transparent substrate (e.g. glass is most frequently applied in optical microscopy). The next step is pattern formation for manufacturing microlenses of a desired diameter. After the development, the polymer is thermally fused due to the heating of the whole structure to the glass phase transition temperature. The surface tension will aid in forming hemispherical lenses (Fig. 10c). The focal length depends on the combination of lens diameter and resist thickness. Other structures that can be fabricated by direct patterning include gratings and plates with Fresnel zones.

The second method of forming waveguides in bulk polymer or quartz glass by applying PBW involves direct-write ion beam modification without a development step [132]. This is achieved by utilizing the process proceeding at the final stage of ion motion in the sample when a buried waveguide channel is created in a substrate. As shown above, ion beams have the unique feature that the amount of energy they deposit into a substrate rapidly increases as the velocity decreases. Towards the end of the range, the probability of an ion creating a vacancy also rapidly increases. The net effect is the creation of a buried region of damage resulting in a local increase in material density, and therefore a local increase in the refractive index. This damaged region can subsequently act as the core of a waveguide.

5. The use of slow positrons for diagnostics of materials

A positron microscope with a microprobe built around it is actually known to a relatively narrow circle of specialists engaged in relevant research with the application of these facilities [133]. The positron annihilation technique has been described in a recent review [198], which, however, does not consider transmission or scanning positron microscopes or the microprobe.

Monitoring defects as a distribution function of defect concentration with depth (defect depth profiling) is possible by varying the energy in a range of a few eV to several dozen keV imparted to monoenergetic positrons upon moderation [134]. Only a small fraction of less than 1% of incident positrons undergoes this moderation process. Once the accelerating potential is specified, the unmoderated positrons must be separated from the beam of monoenergetic positrons that is used for defect experiments. The moderation requires some spatial separation of the positron source and the sample, and thus a beam guidance system must be employed (see Section 5.4 below). The principles underlying defect profile measurements and their application in different slow positron beam techniques are considered in Sections 5.4 and 5.5.

5.1 Positron source and moderation

Figure 11a presents the emission energy spectrum of an ^{22}Na radioactive source. Various materials are utilized as moderators, bearing in mind that energy values equaling the (negative) positron work function can be obtained in many solids. In most cases, a transmission geometry with a moderator thin foil placed directly on top of the source capsule is preferred. The thickness of the foil is much less than the mean positron penetration depth. Therefore, only a small fraction of positrons thermalizes and starts to diffuse there. If the surface is reached during the diffusion, such positrons are spontaneously emitted from the foil with a kinetic energy equal to the thermally broadened work function Φ^+ (Fig. 11b). Materials made from elements with

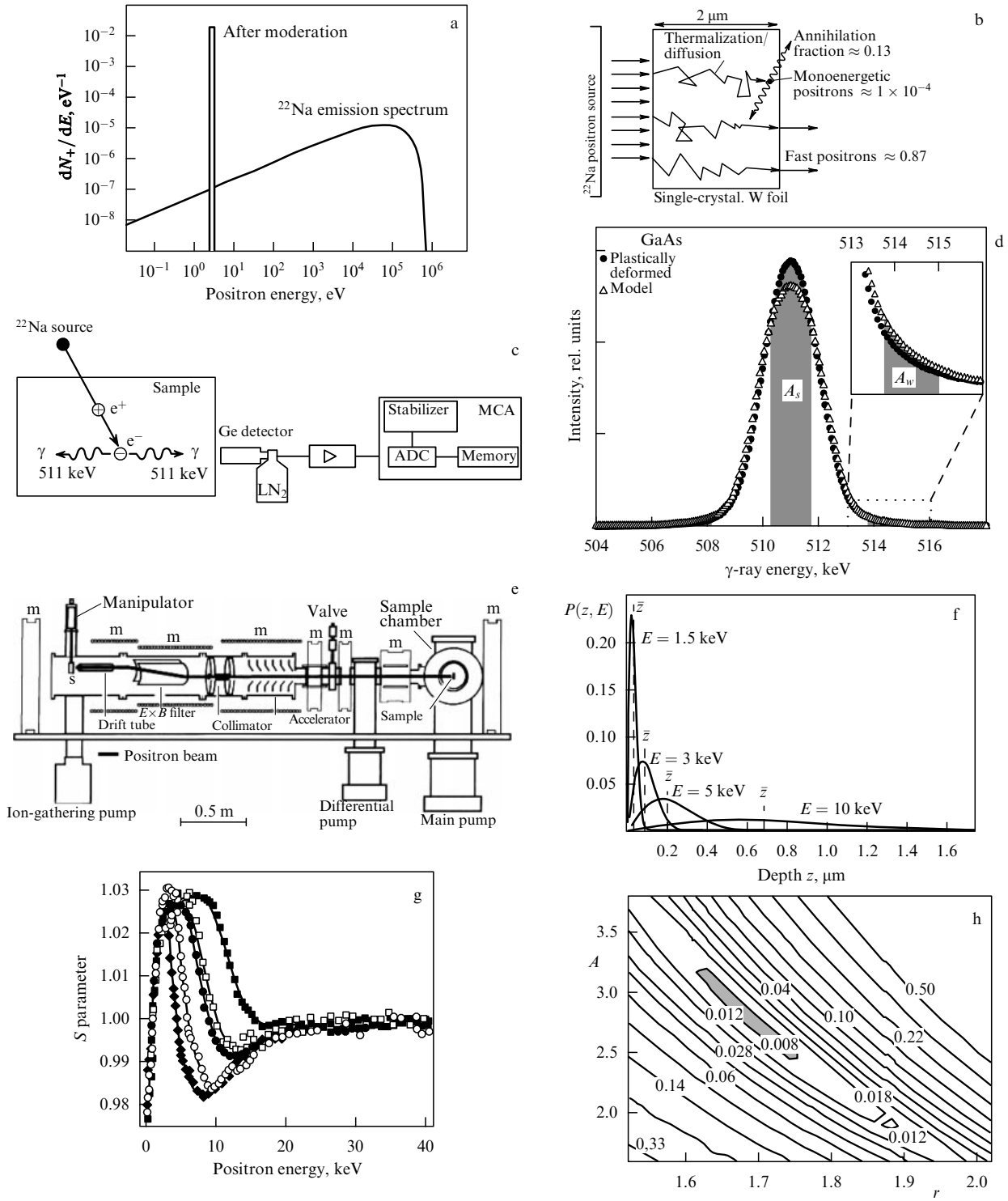

Figure 11. (a) Positron emission spectrum of an ^{22}Na source. dN_+/dE is the number of positrons per energy channel E. The narrow curve centered at 3 eV illustrates the positron energy distribution after moderation in tungsten. (b) Schematic of positron moderation in a transmission geometry by (100)-oriented tungsten foil. Most positrons leave the moderator foil with a high residual energy. A smaller fraction stops and annihilates in the foil. When the surface is reached during diffusion, positrons may be spontaneously emitted due to the tungsten negative work function. The moderation efficiency amounts to $\sim 10^{-4}$. (c) Experimental arrangement for measuring Doppler broadening of the annihilation peak of γ-quanta on the 511 keV line. The signal enters a Ge-detector through the preamplifier, then passes through the analog–digital converter (ADC) to the multichannel analyzer (MCA). (d) Doppler broadening spectrum of the annihilation peak in Zn-doped gallium arsenide illustrates positron trapping in defects of plastically deformed GaAs(Zn). Line shape parameters S and W of the annihilation peak are determined by the areas under the curve, A_s and A_w. The curves for initial and plastically deformed GaAs are normalized to an equal area. (e) Section view of the slow positron beam system (POSSY) at Martin Luther Universitat, Halle-Wittenberg, Germany. Positrons emitted from the source–moderator arrangement (S) are fed to the collimator through the $E \times B$ filter and accelerated to the sample. A circular magnetic field is generated by the guidance coils (m). Vacuum around the source is maintained in the 10^{-6} Pa range. A pressure of order 10^{-9} Pa can be achieved in the sample chamber by stepwise differential pumping of the vacuum system. (f) Makhov profiles $P(z, E)$ in silicon calculated for four energies of incident positrons by formula (6) with parameters $A = 40$ mg cm^{-2} keV^{-r}, $m = 2$, and $r = 1.6$. Dashed lines are fitted to average penetration depth $\bar{z}$. (g) S parameter. (h) Experimentally determined parameters A and r for a Makhov profile (6).

large atomic numbers appear more suitable for moderation due to the increased ratio of the mean diffusion length to the thermalization distance. The most preferred materials for the purpose are a (100)-oriented single-crystalline tungsten foil a few μm in thickness and a (110)-oriented tungsten single crystal to be applied in backscattering geometry.

Since positrons may be trapped in defects during their diffusion to the surface, a foil containing only a small number of positron traps must be prepared by annealing. The work function Φ^+ of positrons from a (110)-oriented tungsten single crystal has been measured previously to be -3.0 eV, and a moderation efficiency of 3×10^{-3} could be achieved (Vehanen et al. [136–138]). The moderation efficiency is expressed as the ratio of the number of moderated positrons to the total number of incident particles. Usually, efficiencies on the order of 10^{-4} can be obtained. Polycrystalline tungsten foils with a much lower moderation efficiency were also successfully tested by Brusa et al. (see references cited in papers [134, 135]).

Furthermore, Kharti et al. [133] in 1990, and Mills and Gullikson [157] in 1986 described solid-state rare-gas moderators obtained by depositing a neon or krypton layer on the carrier foil at low temperatures. Such moderators have an extremely high (up to 10^{-2}) moderation efficiency (a fact that has not yet found a convincing explanation). It is supposed that a drift due to the action of an internal electric field that orients the diffusion motion of individual positrons plays an important role. Another future development may be the use of SiC as an electric field-assisted positron moderator (Bauer-Kugelmann et al., 1977 [140]; Beling et al., 1987 [141]; Brauer et al., 1977; Störmer et al., 1996 (see references in papers [133, 197]). This material is the sole semiconductor known so far with a negative positron work function (electrostatic moderator). The low moderation efficiency requires much stronger sources for positron beam techniques than those used in conventional positron lifetime spectroscopy and Doppler broadening measurements. Moreover, intense radiation protection is needed because the source activity is as high as 5×10^9 Bq (135 mCi).

5.2 Measurement of Doppler broadening of the annihilation peak

5.2.1 Experimental setup. The aforementioned energy broadening of the annihilation line was estimated using an energy-dispersive system of high-resolution detectors (Fig. 11c). Liquid nitrogen-cooled pure Ge crystals of high resolution efficiency (about 20%) were used. Under applied high voltage (positron energy of several keV), annihilation photons cause separation of a charge that is converted in the preamplifier into an electrical pulse. Its amplitude is a measure of photon energy and can be registered after main amplification in a multichannel analyzer. A digital peak-stabilizing system allows the long-term collection of several million counts. The time of the measurement is comparable to the collection time characterizing a positron lifetime spectrum. In this way, the total life span of positrons can be measured. Both techniques can easily be implemented at the same time because the Ge detector should be separated sufficiently from the sample in order to avoid pile-up effects in the detector system.

5.2.2 Data treatment. The influence of positron trapping in defects on the Doppler broadening spectrum $N_D = f(E)$ is demonstrated in Fig. 11d. A quantitative evaluation can be carried out with specific line shape parameters. The S parameter is defined as the area of the central low-momentum part of the spectrum, A_s, divided by the area below the whole curve (A_0) after background subtraction, namely

$$S = \frac{A_s}{A_0}, \quad A_s = \int_{E_0 - E_s}^{E_0 + E_s} N_D \, dE. \tag{4}$$

The W parameter is taken in a high-momentum region far from the line center, as indicated in Fig. 11d. It is calculated as the area under the curve in a fixed energy interval, A_w, divided by A_0:

$$W = \frac{A_w}{A_0}, \quad A_w = \int_{E_1}^{E_2} N_D \, dE. \tag{5}$$

The limits of integration are chosen symmetrically around the energy $E = 511$ keV for the calculation of the S parameter, $E_0 \pm E_s$. The energy limits E_1 and E_2 for the W parameter must be defined in such a way as to have no correlation effects with the S parameter. These chosen limits are kept constant for all spectra to be compared. For the determination of the S parameter, the curves of a defect-rich sample and a sample free of positron traps are plotted in Fig. 11d and normalized to an equal area. The S parameter limits should be taken as the intersection points of both curves to obtain the largest sensitivity to defect-induced changes in the line shape. Often, these limits have simply been taken to give an S parameter of 0.5 for a defect-free material. This means that the determination of W must start at a limit significantly separated from the intersection points of the curves. The limits were set to (511 ± 0.8) keV for the determination of S, and to $(511 + 2.76)$ and $(511 + 4)$ keV for W in Fig. 11d. The ratio between the S parameters for plastically deformed and reference GaAs samples was found to be 1.0695. The corresponding ratio of W parameters was equal to 0.7726.

The background correction is often performed as the subtraction of a straight line. Because the Doppler broadening spectrum of gamma-quantum annihilation radiation is symmetric with respect to 0°, peak tail intensities will be identical. More sophisticated treatments relies on a realistic background distribution simulated by a nonlinear function. This function takes into account that the background at a given γ-ray energy is proportional to the sum of annihilation events with high energies. Despite such a background reduction, the Doppler broadening curve remains slightly asymmetric. The calculation of the W parameter is, therefore, frequently carried out only in the high-energy wing of the Doppler curve. High-quality Doppler broadening spectra are obtained by the coincidence technique, preferably with a setup using two Ge detectors. In this case, W parameters can be taken on both sides of the curve.

5.3 Positron beam guidance systems

A small fraction of monoenergetic positrons leaving the moderator need to be separated from the unmoderated (fast) particles before they can be utilized in experiments. The separation takes place in the beam guidance system comprising an energy filter. This can be accomplished in a magnetic guidance system with the use of external electrodes in an $E \times B$ filter (crossed magnetic and electrical fields, Hutchings et al., 1986 [133, 134]) or by applying external magnetic fields perpendicular to the beam direction (Liszkay

et al., 1992; see references cited in paper [133]). Another simple method relies on the employment of bent solenoids. In this case, unmoderated positrons are stopped by a shield. High-vacuum conditions (10^{-5} Pa) are sufficient for operating the guidance system and for positron studies near the sample surface. An ultrahigh vacuum is needed only for surface exploration. In this case, the specimen chamber should be located far from the differential pumping station.

The magnetically guided positron beam system realized at Martin Luther Universitat, Halle-Wittenberg, Germany is demonstrated as an example in Fig. 11e. The source–moderator arrangement is placed in front of drift tubes, at the ends of which positrons enter the $E \times B$ filter. The monoenergetic positron beam is guided into the system axis and acquires a maximum energy of 50 keV in a linear accelerator. Fast positrons are stopped in the collimator. The positron emission angle with respect to the normal of the moderator foil amounts to a few degrees (Fischer et al., 1986 [142]). The longitudinal magnetic field spreading over the whole beam system forces the positrons onto a helical trace. This ensures that all emitted positrons reach the target. The system of guiding coils (Fig. 11e) generates this longitudinal field.

The beam guiding can also be done by a system of electrostatic lenses (Rosenberg et al., 1980 [133, 134]), the main advantage being the possibility of focusing the beam. The design of such a lens system is, however, rather complicated due to a broad spread in energy in the positron beam.

5.4 Measuring techniques

The Doppler broadening measuring technique can be applied for slow positrons similar to the conventional procedure with foil sources. A Ge detector is mounted close to the sample outside the specimen chamber. The measurement of Doppler broadening becomes possible because the energy of annihilation radiation is high enough to allow the transmission of γ-quanta through a thin stainless steel wall. As explained earlier in Section 5.3, the line shape parameters S and W can be used to identify defects and measure their concentration. In a slow positron system, these annihilation parameters are measured as a function of the positron beam energy, i.e. positron implantation depth. In addition to depth sensitivity, another advantage of a slow positron beam system is the quality of Doppler broadening of the annihilation peak because, in such a geometry of the experiment, neither Compton nor other background radiation is superimposed on the peak, since the generation of γ-quanta in the source does not contribute to the background of the spectra. Furthermore, there is no positron source contribution to the Doppler spectrum present in the conventional technique due to annihilations in the source foil.

The estimation of positron lifetime is a more suitable tool for the identification of valence orbitals of various types of defects and determination of their concentration than the Doppler broadening measuring technique. The conventional setup with start-up and stop detectors is not applicable in a slow positron beam system because of the low strength of the source at which the emission of γ-quanta (see Section 5.3) cannot be correlated with annihilation events in the sample. Moreover, the positron time of flight is much longer than the lifetime in the sample. Thus, the measurement of positron lifetime is only practical by pulsed beams supplying the start pulse with the help of a specially designed focusing system. Such a technique is electronically expensive and has been realized up to now only in a few laboratories, e.g. in Münich (Kögel et al., 1996, 1998 [143, 144]) and Tsukuba (Akahane et al., 1990 [145]). The performance limit of pulsed positron beams was discussed by Sperr and Kögel in 1997 [135].

In addition to lifetime and Doppler broadening measurements, two-dimensional angular correlation of annihilation radiation can be measured in a slow positron beam setup. An advantage here consists in the possibility of analyzing the electronic structure of the surface layers, thin epitaxial layers, or interfaces (e.g. Howell et al., 1985; Peng et al., 1996) [133, 148].

The density of defects can be determined with a slow positron beam system in a back diffusion experiment, in addition to the measurement of the momentum distribution and positron lifetime. The fraction of positrons diffusing back to the surface, f_s, can be determined via annihilation parameters on the surface or the relative amount of positronium formed near the surface. This becomes possible because the surface annihilation parameters usually differ from those in the bulk, and positronium can be formed only at the semiconductor surface. The relative number of back-diffused positrons is a function not only of their implantation depth and the diffusion coefficient but also of the concentration of defects. This is due to the fact that trapped positrons cannot reach the sample surface. Quantity f_s is measured as a function of the incident positron energy. The relevant fitting routine makes it possible to calculate the trapping rate as a function of the depth. The main disadvantage of this procedure is that it provides no information on the nature of positron traps. Parallel measurements of a positron lifetime and Doppler broadening are also recommended. On the other hand, the overall trapping rate for all positron traps can be deduced from the results of back diffusion experiments. Hence, defect concentrations can also be determined in positron-saturated regions, i.e. at very high concentrations, as was demonstrated for ion-implanted silicon by Eichler et al. in 1997 [133].

5.4.1 Defect depth profiling. In order to obtain a defect depth profile from the measured variation of annihilation parameters as a function of the incident positron energy, knowledge of the positron implantation profile is required. The profiles resulting from Monte Carlo simulations and experimental results are presented in the next section. The computation of defect depth profiles is nowadays carried out with computer programs. These procedures are also described in Section 5.4.2.

5.4.2 Positron implantation profiles. Variations of the positron energy allow determining the concentration of defects as a function of the penetration depth z, i.e. the measurement of the defect depth profile. The implantation and penetration profiles $P(z, E)$ of monoenergetic positrons having the energy E are given as

$$P(z, E) = \frac{m z^{m-1}}{z_0^m} \exp\left(- \left(\frac{z}{z_0} \right)^m \right), \tag{6}$$

where

$$z_0 = \frac{A E^r}{\rho \Gamma(1 + 1/m)},$$

m, r, A are empirical parameters, ρ is the sample mass density, Γ is a gamma function, and $\bar{z}$ is the mean penetration depth

defined as

$$\bar{z} = \frac{AE^r}{\rho} . \quad (7)$$

The widely used empirical values are $A = 4.0$ mg cm^{-2} keV^{-r}, $m = 2$, and $r = 1.6$ (Vehanen et al., 1987) [138].

The positron implantation profile is called a Makhov profile, named after Makhov's original electron implantation experiments (Makhov, 1961; see references cited in monograph [133]). The parameters of this profile can be obtained theoretically from Monte Carlo simulations (Valkealahti and Nieminen, 1986, 1984 [146, 147]). Ghosh (1995) [133, 148]) showed by a set of Monte Carlo calculations that the parameters A and r are material-dependent. The positrons after thermalization, i.e. at the beginning of diffusion, exhibit a depth distribution as given by formula (6). Examples of such Makhov profiles are exhibited in Fig. 11f. The limitations on measuring defect depth profiles for high positron energies become apparent as well-pronounced defect structures lying relatively deep in the sample are smeared out when superimposed by the positron diffusion profile. Ghosh (1995) [148] obtained different A and r values, depending on the Monte Carlo methods used. Although the main features of the positron implantation profile could be described by the analytical Makhov profile, small deviations were found. These deviations necessitated approximation of the profile thus obtained by parameterizing function ξ (Ghosh and Aers, 1995) [150].

The empirical parameters of the Makhov profile (Fig. 11f) were also determined in experiments by Gebauer et al., 1997; Leung et al., 1995 [151, 153]. Their results are presented in Fig. 11g. Parameters of the implantation profile were deduced from the E-dependence of S for amorphous Si layers, with the sample thickness being determined independently by studying the cross section in a scanning electron microscope. The 120–1000-nm thick a-Si layers were grown by molecular beam epitaxy on a buffer SiO_2 layer prepared by thermal oxidation at 1000 °C. The curves for the S parameter were fitted by the VEPFIT software package using systematic variation of A and r parameters of the Makhov profile [139]. For each (A, r) pair, the standard deviation ξ was calculated based on the deviation of the layer thickness obtained from the fit of the positron annihilation data, z_i^{fit}, and the thickness measured by scanning electron microscopy, z_i^{SEM}:

$$\xi = \frac{1}{5}\sum_{i=1}^{5}\left(\frac{z_i^{\mathrm{SEM}} - z_i^{\mathrm{fit}}(A,r)}{z_i^{\mathrm{SEM}}}\right)^2 . \quad (8)$$

Deviation ξ is averaged in formula (8) over all five measured $S(E)$ profiles (Fig. 11g). Gebauer et al. (1997; see references cited in paper [151]) found a minimal deviation for Makhov profile parameters $A = (2.75 \pm 0.25)$ mg cm^{-2} keV^{-r} and $r = 1.7 \pm 0.05$ (Fig. 11h). These parameters are in good agreement with the results of the Monte Carlo simulation by Ghosh in 1995 [148].

Calculations of ξ took into account all five curves plotted in Fig. 11g. The minimal deviation is indicated by the shaded area in Fig. 11h at point $A = (2.75 \pm 0.25)$ mg cm^{-2} keV^{-r} and $r = 1.7 \pm 0.05$ (Gebauer et al., 1997 [151]).

5.5 Computation of defect depth profiles

Trapping of positrons by defects can occur after their thermalization during diffusion. The diffusion of positrons is usually described by Fick's second law. To calculate defect depth profiles, only the one-dimensional diffusion equation has to be solved.

Possible variables describing a given measurement of annihilation peak Doppler broadening are the line shape parameters (S or W), while for the positron lifetime measurement these are lifetime components τ and their intensities I_i, or the so-called positronium fraction F. The profile of these annihilation parameters in terms of the depth is the defect distribution profile in the sample, represented as the convolved expression describing the penetration profile $P(z, E)$ and influenced, in turn, by positron diffusion. The profile of positrons absorbed by the material is smeared out due to superposition of the positron diffusion profile. The diffusion equation must be solved numerically. However, the defect depth profile can hardly be identified directly. For following the numerical procedure, the sample is usually divided into slices thin enough to assume a constant defect concentration and positron density there. The annihilation parameters are fitted as a function of energy in a nonlinear procedure. In this way, the defect distribution perpendicular to the sample surface is obtained.

The VEPFIT is a program package for the evaluation of slow positron beam data found in experiments (van Veen et al., 1990, 1995) [133]. The Gaussian curves are an analytical function of a defect profile or a thin slice structure with a constant defect concentration, regarded as the input data for special programs. Both the Gaussian and the step function of the defect concentration, distribution can adequately describe experimental findings. Not infrequently, it is impossible to decide which function is a better choice to describe the real defect profile. This is due to the broad positron implantation profile and the positron diffusion as a function of the defect concentration.

Another algorithm (POSTRAP program) for the evaluation of slow positron depth profiles with the aim of measuring the distribution of defect concentrations is presented in the work of Ghosh and Aers (1999) [150]. The program permits estimating the influence of defects and an electric field on positron diffusion. This, in turn, allows arbitrary forms of positron implantation profiles to be obtained.

An example of the determination of a defect profile is given in Fig. 12a, b. The S parameter was measured as a function of the positron implantation energy in arsenic-doped silicon (Gebauer et al., 1997) [151]. The data were fitted by VEPFIT assuming a structure of four slices with different defect densities or a normal (Gaussian) defect distribution. The layer structure presented in Fig. 12b exhibited the best results of fitting (Gebauer et al., 1997 [151]).

These computer programs also provide information on the fraction f_s of positrons diffusing back to the surface. The back diffusion experiments have the advantage that the positron trapping rate can also be determined in the case of saturated capture, in contrast to the conventional techniques described in Sections 5.4 and 5.5.

This implies that there is, in principle, no upper sensitivity limit for a given method. However, the lower limit is comparable to that in conventional techniques due to the limitations imposed on the minimum fraction of positrons annihilating from defects. The annihilation fraction η can be calculated from f_s as a function of the incident positron energy, i.e. the depth distribution profile:

$$\eta(E) = 1 - \frac{f_s(E)}{f_s^{\mathrm{ref}}(E)} , \quad (9)$$

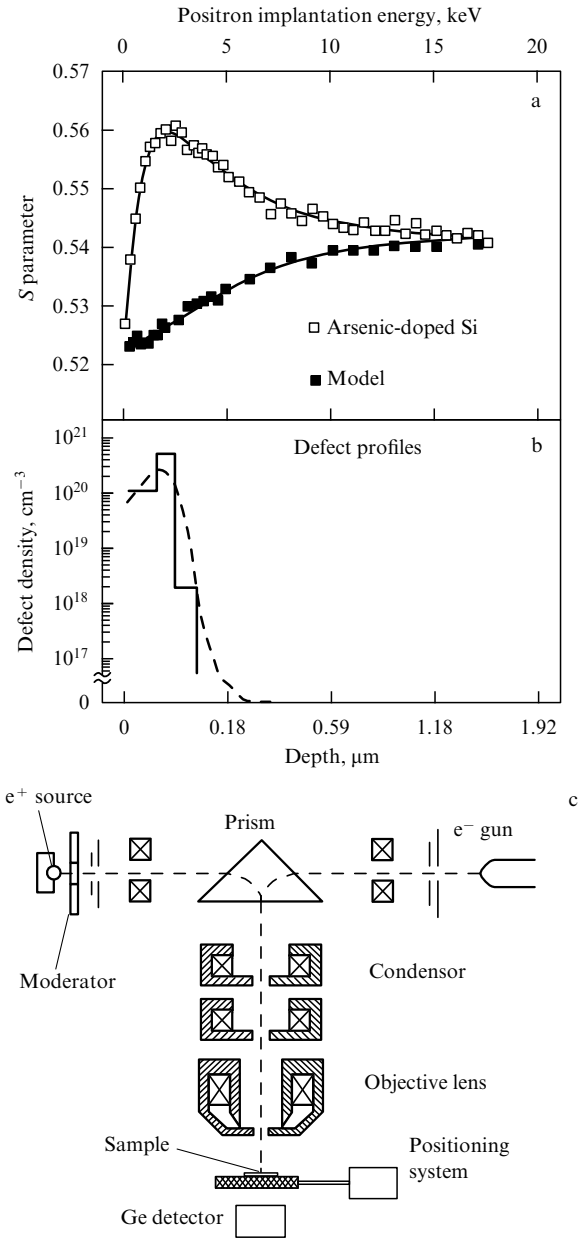

Figure 12. (a) *S* parameter as a function of incident positron energy for an arsenic-doped Si sample at a fluence of 5×10^{13} cm^{-2} (60 keV). The experimental curve was fitted by VEPFIT in terms of positron energy variation. The observed and fitted data for an Si sample free of traps are presented as a standard. (b) The model to be fitted is a structure of four slices with different defect densities or a Gaussian defect distribution. The structure of the layer that yielded the best fitting results is presented (Gebauer et al., 1997 [151]). (c) A combination of a scanning electron microscope (Zeiss/Leo) with a positron microprobe realized at Bonn University (Greif et al., 1997; see references cited in paper [171]). A positron beam is guided through the optical axis of the microscope. An electron beam is used to select the area of interest for Doppler broadening measurements.

where $f_s(E)$ is the quantity characterizing the sample under consideration, and $f_s^{ref}(E)$ is the corresponding back diffusion fraction in a defect-free reference sample (Mäkinen et al., 1986) [133].

5.6 Positron microscopy and microprobing

The experimental methods considered in the preceding sections have recently been supplemented by new positron spectroscopic technologies, even though some of them are still in the development phase or have restricted applications to defect studies. In what follows, we briefly consider them to give an idea of their potential value.

The application of the slow positron beam technique (Section 5) is restricted only by its spatial resolution. The development of positron beams with enhanced brightness and focusing precision would permit studying materials with the help of a positron microscope or microprobe (see Section 5.7 below).

The first transmission positron microscope (TPM) was realized by van House and Rich in 1988 [133, 137]. They achieved a magnification of 55 in transmitting positrons through a polymer foil. The TPM may have a variety of new applications compared with the transmission electron microscope (TEM). The comparison of the contrast formation in a TPM and TEM may provide valuable information about concrete elements over the effective reflection area. The reduced small-angle scattering of positrons is governed by the much more effective screening of the nuclei. A strongly Z-dependent (Z is the atomic number) difference in the amplitude contrast exists between electron and positron microscopies. Thus, a comparison of the contrast mechanisms for both techniques could provide important chemical information on the properties of materials.

The positron re-emission microscope (PRM) utilizes effects of the negative positron work function on certain surfaces (see Schultz and Lynn, 1988 [152]). The surface of a sample is exposed here to a positron beam with an energy of several keV. The penetrating positrons thermalize and diffuse; as a result, many of them reach the surface. The lateral distribution of re-emitted positrons is used to form an image with the aid of a position-sensitive detector, such as a multichannel plate [153]. A dark contrast appears in this image when near-surface defects prevent positrons from emission. Thus, PRM makes up an extremely sensitive tool for the detection of positron-active defects on the surface and in the near-surface region. Such a microscope was realized in reflection geometry by van House and Rich (1988; see references cited in book [133]). They achieved a spatial resolution of 2.3 μm.

Positron microscopy is still technically underdeveloped. Its main drawback is the lack of a positron beam with the sufficient brightness. The spatial resolution is limited because positron point sources are unavailable.

A promising development at Bonn University, Germany, involves the combination of a scanning electron microscope and a positron microprobe. SEM images were used to select areas of interest on the sample surface for subsequent positron measurements with higher lateral resolution. For this purpose, a monoenergetic positron source was integrated into the optical system of a commercially available scanning electron microscope (Greif et al.,1997; see references cited in monograph [133]). An electron gun was replaced by a magnetic prism for energy filtering of positrons. Electron and positron beams were guided through the prism with the same magnetic field on the optical axis of the microscope (Fig. 12c).

5.7 Principles of positron beam generation

Within a few years, the high-frequency low-energy positron beam has become a powerful tool for spectroscopic analysis of defects based on the measurement of positron lifetime in the near-surface layer [155–157]. Positrons emitted from a radioactive source thermalize in a thin layer of single-crystalline tungsten and are re-emitted with an energy close to 3 eV and overall efficiency of around 2×10^{-4}. The re-emitted

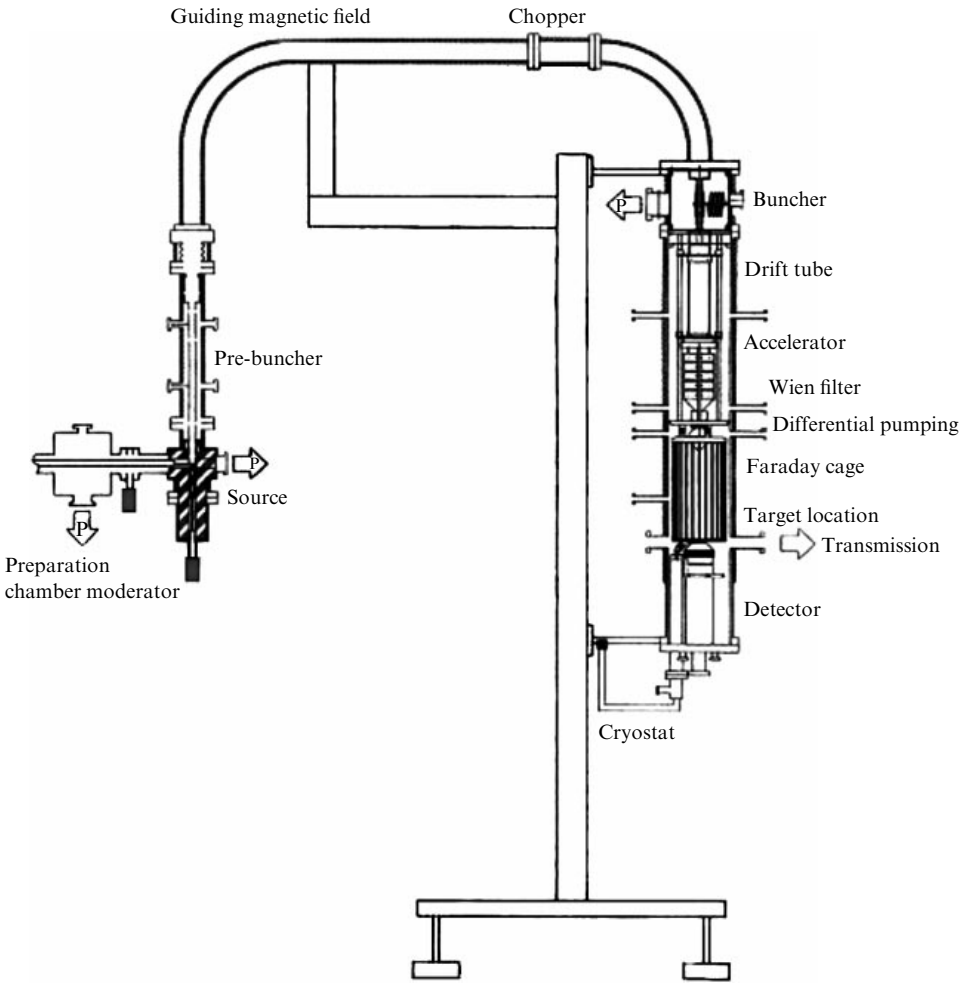

Figure 13. Schematic of the upgraded generator of low-energy pulsed positron beams.

positrons make up a continuous beam. It is compressed to a 100-ps pulsed beam near the target using special RF (HF) devices. Timing signals for lifetime measurements come from one of the annihilation photons, while the respective synchronizing signals are generated by the RF system. The diameter of the positron beam in such a system was about 4 mm. The first system of this type was put into operation in 1988. It allowed measuring the lifetime depending on the positron energy, i.e. penetration depth. The system was modified in 1993 to improve the quality of lifetime spectrum measurements (by decreasing the contribution from background signals, as well as the level of backscattering signals) and to increase measurement intervals up to 20 ns to achieve the best filling factor [154]. Moreover, such a system permitted measurements at variable temperature.

The system has a chamber for *in situ* annealing of a single-crystalline tungsten foil and a pre-buncher to compress the continuous beam to pulses of a 1.7-ns half-width at the half-height by applying sawtooth voltage to the drift tube. More details can be found in paper [155]. The system has been further improved recently (Fig. 13). The distance between the positron source and the detector was increased to reduce the level of background signals, and a chopper was installed at the beamline behind the device. The new, main 50-MHz buncher installed at the drift tube and the accelerator were subsequently moved away from the target, thus leaving a greater space in front of the sample chamber to reduce the positron backscattering effects.

The built-in Wien filter prevents the return to the surface of positrons backscattered at the angles of less than 90°. Differential pumping ensures a vacuum down to 10^{-10} mbar around the target. Furthermore, the recently introduced system for the substitution of samples makes it possible to study a few without disturbing the vacuum conditions. The new temperature control system allows the sample temperature to be varied from 10 to 600 K. The horizontal position of the sample chamber permits studying liquid materials, particularly liquid metals and alloys. The system has one more advantage over conventional methods, besides the possibility of measuring positron lifetimes as a function of the energy (i.e. penetration depth). Specifically, it is free of limitations on positron intensities due to accidental coincidences. One of the timing signals comes from the HF system, and the final coincidence level is equivalent to the detector count rate for annihilation photons (integrated rate) with this timing signal. In the case of a highly intense main positron source, the count rate can be increased almost without limit.

5.8 Experimental results obtained with the use of pulsed beams

Figure 14 presents typical average positron lifetimes depending on implantation energy E and penetration depth $z_1(E)$. The different shapes of the curves in Fig. 14a are due to back diffusion and surface effects. Two n-type Si specimens with an impurity concentration of 10^{15} cm^{-3} were investigated. The mean positron lifetime τ_m for both samples at implantation

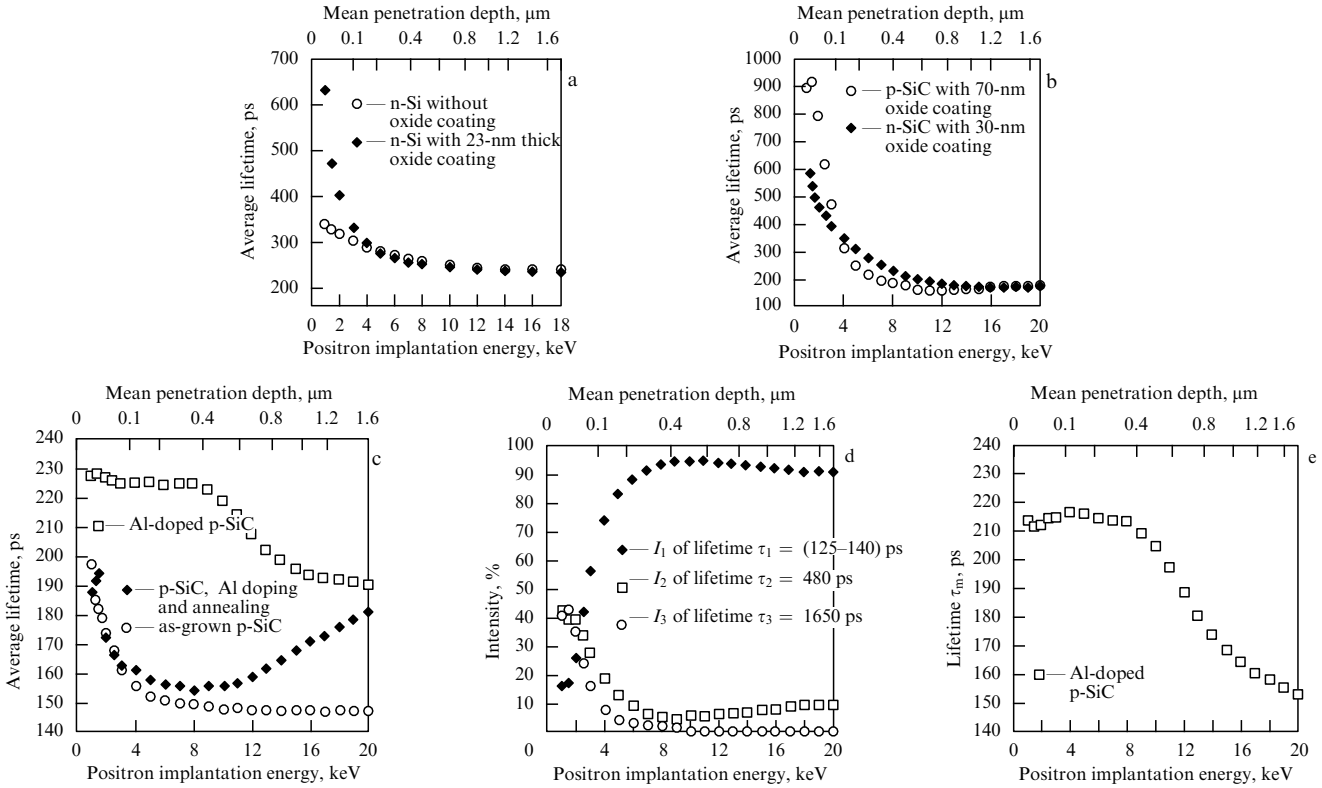

Figure 14. (a) Average positron lifetime in n-type Si with and without an oxide layer plotted vs positron implantation energy and mean penetration depth. (b) Average positron lifetime in n- and p-type SiC with an oxide layer of different thicknesses plotted vs positron implantation energy and mean penetration depth. (c) Dependence of the average positron lifetime in p-type SiC after Al implantation and subsequent annealing on the mean penetration depth. Results for the as-grown specimens are presented for comparison. (d) Dependence of the shortest lifetime (τ_1) in Al^+-doped SiC samples on positron implantation energy. Lifetime of the second component $\tau_2 = 480$ ps. (e) Dependence of average positron lifetime in p-type SiC shown in figure b on positron implantation energy and mean penetration depth.

energies higher than 5 keV was practically identical and assumed to be constant. The values of τ_m differed significantly at lower energies. The measured lifetime spectra for Si specimens from which the surface oxide layer was stripped off were amenable to analysis only with the employment of two lifetime components with intensities of 385 and 225 ps, respectively. The intensity of the larger component decreased roughly to 75% (to 10% at an implantation energy of 18 keV) due to the probability of positron back diffusion toward the surface. A lifetime of 385 ps is, as a rule, indicative of positron annihilation near the surface [157–162]. A shorter lifetime, 225 ps, is characteristic of defect-free single-crystalline silicon. The mean lifetime in the oxide layer at the surface of an Si single crystal increases to 1650 ps at low implantation energies. The analysis of lifetime measurements revealed its three components: 1350, 450, and 225 ps with appropriate intensities. Evidently, the largest lifetime corresponds to positronium (Ps) formation in the oxide layer. The value of 450 ps is attributable to the presence of pores in the oxide layer and at the oxide–single crystal interface, whereas the positron lifetime of 225 ps is characteristic of the bulk silicon single crystal. Figure 14d, e depicts positron lifetimes for 4H-SiC specimens differing in the degree of doping and the thickness of the oxide layer (30 and 70 nm, respectively).

In doped n-type specimens, back diffusion to the surface is similar to that in doped SiC p-type samples, which can be explained by the negative charge of free carriers. It is especially apparent in an energy range of 4–12 keV. In both samples, positronium forms in the oxide layer. For the latter sample, the lifetime spectrum was adjusted (approximated) to fit the three lifetime components with the respective intensities. The results are given in Fig. 14c.

An orthopositronium lifetime signal from the detector was observed only in the 70-nm thick oxide layer; its intensity rapidly decreased with decreasing implantation energy. The lifetime component τ_2 corresponds to vacancy type clusters (most likely microtubes) produced in the course of crystal growth. The intensity I_2 of the second lifetime component remains low (roughly 10%), notwithstanding high implantation energies. The shortest lifetime τ_2 is characteristic of bulk single crystals and decreases due to positron trapping in defects and surface states, especially at low implantation energies. SiC appears to be a promising material for nuclear radiation detectors operating at high temperatures [161]. However, fabrication of such devices requires local modification of the degree of doping. The long range of impurity diffusion necessitates the employment of high treatment temperatures in excess of 2300 K that cause SiC decomposition [162, 163]. Ion implantation may be an alternative modality, since it allows low-temperature processing and plate structuring [164]. However, these procedures do not prevent the formation of radiation defects. The post-implantation defects were studied after their annealing by measuring lifetimes for various 4H-SiC specimens in the form of a 4-μm thick epitaxial layer of p-SiC grown on an SiC n-type substrate with a degree of doping equal to 7.3×10^{18} cm^{-3}. Al impurities were implanted at five different energies and a total fluence of 2.35×10^{13} cm^{-2} to obtain a uniform implantation profile. The results are demonstrated in Fig. 14e.

The average positron lifetime after implantation and annealing was compared with the results of measurements in an SiC bulk crystal with p-type conductivity. The average lifetime τ_m in this sample increased at the lowest implantation energies due to annihilation in the surface states. As the energy increased, τ_m rapidly dropped to 141 ps; such behavior is typical of bulk single crystals and agrees with theoretical predictions.

The results of measurements for Al^+-doped samples were altogether different. The lifetime was 218 ps at positron implantation energies from 2 to $\sim$ 10 keV (Fig. 14e), suggesting saturation trapping in the defects resulting from the implantation of Al^+ ions.

The results of these measurements are very similar to the calculated lifetime value of 216 ps obtained for divacancies V_{Si}, V_c [66]. The lifetime τ_1 for the sample presented in Fig. 14e is not typical of bulk single crystals. In all probability, it is the integrated result of the measurements (signals) obtained for the bulk material and induced defects. The defective and implanted regions fully recovered after annealing. The lifetime of annihilated positrons (494 ps) is slightly longer than that in as-grown samples (480 ps). The cause of τ_m growth at an energy above 10 keV remains to be elucidated. This feature was observed only in epitaxial samples and may be attributed to the peculiarities of growth and/or p–n junction effects.

5.9 Scanning positron microscope

The natural step after the generation of a pulsed positron beam a few millimeters in diameter is to reduce the diameter to a few microns. The scanning positron microscope (SPM) takes advantage of a positron beam of a micron-scale diameter with variable energy. The SPM is a combination of a conventional scanning electron microprobe and a pulsed positron microprobe with the pulse duration around 100 ps and the spot of size 1 micrometer.

Visualization with an electron beam provides a conventional image of the surface. The areas of interest can be selected on such image in a nondestructive mode for subsequent nondestructive study and analysis with the aid of a positron microprobe [166–168]. This method is based on the results of positron beam research and recent developments in the field of particle optics. The fundamental difference between the systems with electron and positron beams consists in the flux density of their sources. The flux density of a typical LaB_6 source of electrons is 16 orders of magnitude greater than that of a monoenergetic positron beam. However, the employment of an intense positron source improves this ratio by several orders of magnitude [169]. Therefore, the probe-forming strategy for a scanning positron microscope must be that which maintains the positron flux as much as possible, in contrast to the typical probe-forming strategy for a scanning electron microscope, which is based on narrow apertures and corresponding intensity losses. This means that scanning positron microscopy has to apply re-moderation. Furthermore, the development of the SPM must focus on such critical problems as sufficient spatial and time resolutions, effective utilization of positron radiation, sufficient stability of functioning mechanical and electrical systems, low magnetic background, and an appropriate size of the specimen chamber. The general layout of the setup is presented in Fig. 15a.

This system operates in an ultrahigh vacuum of 10^{-9} – 10^{-10} mbar. Specimens with dimensions of up to $20 \times 20 \times 3$ mm are inserted into the chamber through the use of a manipulator. Any region of a specimen can be positioned with the manipulator within the positron- and electron-scanned area of at least 600×600 μm without detriment to

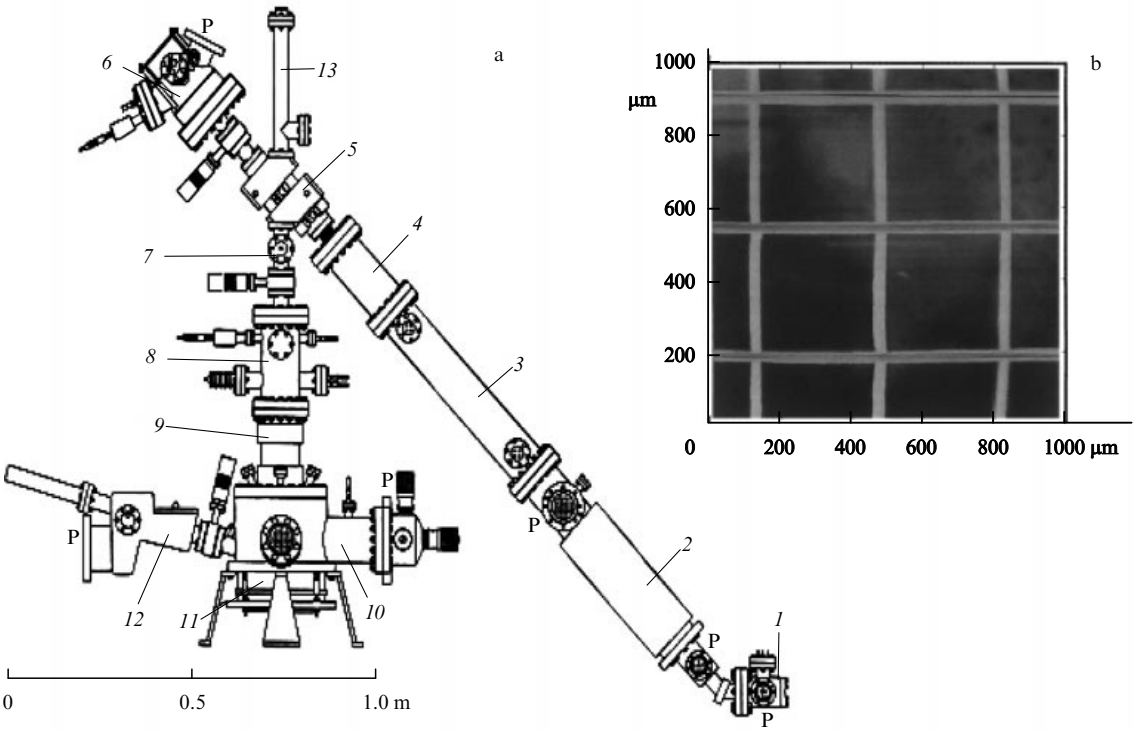

Figure 15. (a) Schematic of the scanning positron microscope: *1* — positron source and moderator, *2* — drift tube for (sawtooth) pulse formation, *3* — first buncher, *4* — accelerator, *5* — beam switch, *6* — re-moderator block, *7* — second buncher, *8* — main accelerator (0.5–30 keV), *9* — scanning (deflecting) coils, *10* — sample chamber with manipulator, *11* — probe-forming lens with detector on the bore central axis, *12* — load lock, *13* — electron gun, P — pumping port. (b) Electron image of a gold mesh of 360-μm spacing and 30-μm bar width.

spatial resolution. The positron source moderator assembly coupled with the first accelerator produces a continuous positron beam of 20-eV kinetic energy. This beam is injected into the drift tube to which a sawtooth signal with a repetition rate of 50 MHz is applied. Positrons in each 20-ns segment of the continuous beam are in this way compressed into bunches approximately 2 ns wide. The compression in the drift tube is much more efficacious than the usual beam splitting, where the losses amount to 30% compared with $\sim 10\%$. After leaving the drift space, the positrons are accelerated to 800 eV by the sinusoidal buncher (resonator). The first buncher is designed by analogy with that used earlier in Ref. [171]. The beam noise damper positioned in front of the buncher suppresses the time-uncorrelated background due to positrons outside of the prebunched pulse. The first buncher increases the pulse width from 2 to 200 ps by means of the re-moderator comprising a W crystal cooled in a cryostat to the liquid-nitrogen temperature (80 K). The cooling leads to a three-fold decrease in the energy spread of re-moderated (re-emitted) positrons, which finally reduces to 40% at the spot diameter. Positron experiments planned for the near future have the objective to cool the tungsten crystal to liquid-helium temperature in order to further decrease the positron's transverse energy spread.

The optical system of the re-moderator block consists of a combination of electric and magnetic lenses focusing the input parallel positron beam onto the moderator and guiding the re-emitted moderated positrons as a parallel beam with a kinetic energy of 200 eV [170, 171]. In order to separate the input and re-moderated beams and guide the lagging one into the optical column, the system contains a toroidal reflector [170, 171]. The optical column consists of an accelerator to ensure an implantation energy in the range from 0.5 to 30 keV, deflecting coils, a sample chamber, and probe-forming magnetic lenses.

At the input of the accelerator, the pulsing beam enters a large Faraday cage (inside the sample chamber) and the magnetic field of the probe-forming lenses being at the potential corresponding to the final implantation stage. The toroidal windings of the reflector for the magnetic field governing the scanning beam are installed outside the vacuum chamber. Because of a large variety of measuring techniques using a positron beam, the specimen chamber of the SPM must differ completely from that in a scanning electron microscope. In order to obtain a high count rate of annihilation photons, a large-area detector must be positioned as close as possible to the specimen chamber. On the other hand, the half space of the chamber forepart must be free of material in order to suppress possible distortions of the lifetime spectra by annihilation radiation resulting from backscattered positrons annihilating at the wall of the vacuum chamber. The necessary design requirements are met by a side-gap single-pole lens placed behind the specimen chamber just outside of the vacuum chamber with the radiation detector inside the central field pole piece [171].

A BaF_2 crystal scintillation counter is fitted directly on a Valvo-XP-2020Q photomultimeter used as the detector of 511-keV positrons. The size of the pulsed beam spot in the re-moderator decreases to 20 μm. The phase-space density of the positrons re-emitted from this spot exceeds that in one of the first moderators by a factor of 3×10^4. Up to now, the typical gain in phase-space density of a single re-moderation stage has been only 20 [134, 171], meaning that in the design of this SPM a single re-moderation stage replaces the three conventional re-moderation stages necessary in other methods [134, 166, 171], thereby reducing the primary source intensity by a factor of 25. This progress in beam quality is due to the well-balanced positron beam transport system, the superior properties of the single-pole lens, and the application of time bunching. It increases the transfer coefficient in the phase space by a factor of 50.

An electron beam which passes the same optical column as a positron beam provides an image that can be used as a readily available important reference for the chosen region to be further scanned by the positron beam. This approach ensures perfect focusing and alignment of the optical column. An electron-beam image of a gold mesh is presented in Fig. 15b.

Actual beam formation (bunching) and re-moderation efficiency are 70 and 23%, respectively; the spatial resolution of the positron beam measures 1 μm. This value is slightly higher than for the electron beam. For practical applications, a preliminary positron source is needed to ensure an acceptable measurement time. A typical lifetime spectrum contains as high as 10^6 counts. It is planned to employ 1-Ci ^{58}Co as the preliminary source of positrons; given the aforementioned efficiency, it is expected to have 5.8×10^5 positrons per second at the target, and 2×10^4 s^{-1} at the annihilation photon detector. For a highly intense positron source, such as the one installed in the reactor [67, 171], the rise may be as high as three orders of magnitude.

Worthy of note is the most successful application of a proton beam microprobe (the PIXE method) and a positron beam microprobe for the analysis of segregation and diffusion processes at micrograin boundaries [172, 173].

The authors of Refs [172, 173] implanted Al^+, C^+, and Ti^+ ions into polished α-Fe specimens at a fluence of 2×10^{17} or 5×10^{17} cm^{-2} and analyzed impurity segregation regions, grain boundaries, and regions of vacancy clusters with interstitial carbon atoms (2.3 atoms); in other words, defect complexes (a vacancy plus a few interstitial C atoms) were examined. The same α-Fe specimens irradiated by high-current electron beams with a different number of pulses were used in paper [173] to analyze the segregation of C atoms and diffusion of Fe vacancies. Interstitial C atoms bunched together in high-carbon regions, where subsequent irradiation with a high-current electron beam caused crater formation resulting in the considerable alteration of the surface relief for the polished α-Fe specimens [172, 173].

The pulsed positron beam and the scanning positron microscope described in this section are the first such currently operating systems. Both are designed not only to demonstrate phenomena (principles) but also to be used in a variety of practical applications. These developments open up new prospects for micro- (and smaller)-scale near-surface research of special interest for solid state physics, materials science, and investigations of nanomaterials, first and foremost nanocomposite, superhard, and thermally stable coatings [174].

6. Near-field microwave diagnostics of materials and media

Near-field microwave diagnostics is a direct nondestructive method providing information on the surface and near-surface properties of various media. It is based on recording the microwave fraction of an impact in the probe near-field, thereby allowing a significant improvement in the spatial

Table 3. Modern microdiagnostic techniques.

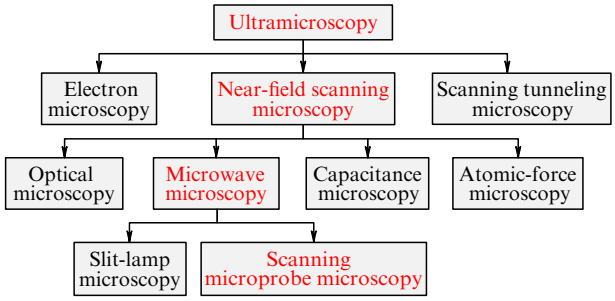

resolution and overcoming the diffraction limit for given frequencies [175–179].

Localization of a microwave signal in the near-field is accomplished using devices whose design and operation principles are considered below. The main factors determining the spatial resolution and accuracy of measurements (signal/noise ratio) are the design of the measuring device, properties of the material being studied, probe size, and distance between the probe and the sample surface. The data obtained are treated by elaborate methods of mathematical physics and numerical analysis, with the involvement of experimental techniques for the diagnostics of materials in the microwave range [175–179].

Table 3 presents the classification of ultramicroscopic (nanoscale) methods, highlighting near-field scanning, microwave, and microprobe microscopies. High resolution is achieved by virtue of a special design of measuring transducers (MTs). Classification of MTs for microwave diagnostics as presented in Table 4 categorizes them into two main classes, resonator and wave systems, which are, in turn, subdivided into subclasses. The following notations are specified in Table 4: IDR — internal dielectric resonator (DR), MDR — microwave DR, ODR — open DR, MS — translation stage, NFI — near-field interaction, SE — sensitive element, CME — coaxial measuring equipment, and COR — cylindrical open resonator.

Near-field microwave diagnostics is extensively invoked to study the surface of dielectric and semiconducting films, to map material permittivity, to detect minor defects and irregularities, and to analyze nonlinear characteristics. It finds wide application in biology and medicine. The application of microwave waves in biological research has important advantages over the employment of visible and IR wavelengths due to their high penetrating capacity (from a few millimeters to decimeters). It permits exploring not only superficial layers but also deep-lying ones (at the expense of the respective loss of spatial resolution on the surface). This property is used to analyze and visualize structures of such biological objects as neoplasms [176, 178].

Equally promising are microwave studies in semiconductor micro- and nanoelectronics because they provide multiparameter information about surface and near-surface layers. An important field for the application of microwave diagnostics is microwave microscopy in nanotechnologies, which is currently employed in the fabrication of high-temperature superconductors, visualization of surface conductivity distribution, local measurement of nonlinear microwave response, etc.

Figure 16a depicts different types of measurement converters, viz. coaxial MT, composite resonator type MT (RMT) with an enhanced Q factor, and stripline MT [179]. Figure 16b presents the schematic layout of a microwave microscope.

The main advantage of microwave near-field microscopy is that it is a multifunctional technique giving the possibility of additional manipulation of the specimen, e.g. by applying constant electric field and magnetic field, an additional microwave field, mechanical and force fields, etc.; what is especially important is that it allows comprehensively studying the properties of surface layers in the microwave range.

The physical principles of the scanning microwave microscopy (SMWM) for semiconductors were developed in Ref. [176] in conjunction with the general concept of enhancing its spatial resolution (at the 100-nm level) and sensitivity (multiparametricity). The concept consisted in the

Table 4. Classification of MTs for microwave diagnostics.

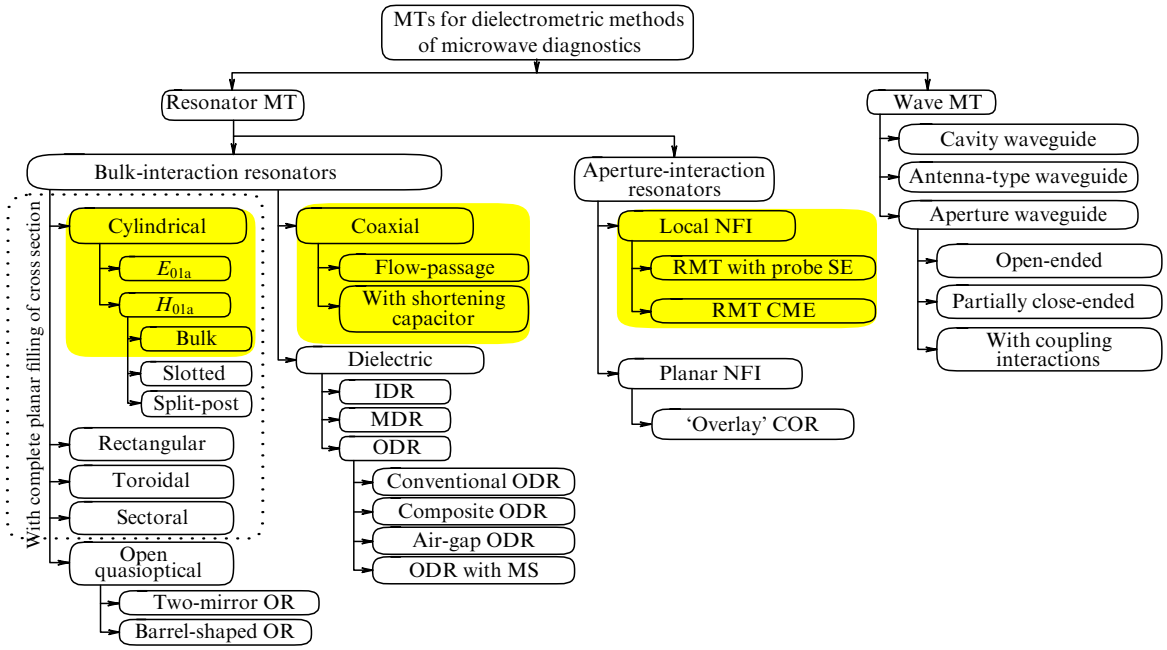

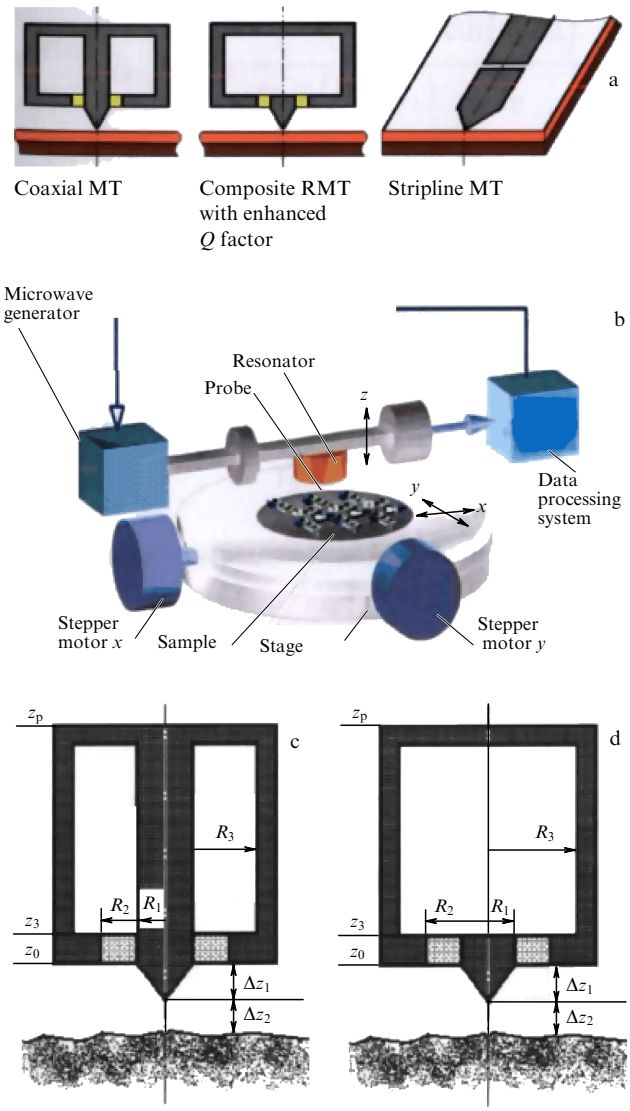

Figure 16. (a) Different types of measuring transducers. (b) Schematic layout of a microwave microscope. (c, d) Geometric diagrams of RMTs for a microwave microscope.

maximum spatial localization of the probing microwave field energy in the electric constituent of the coaxial resonator microprobe, which is normal to the test object; it also consisted in the formation of scanning signals with a wide application of modulation principles and their additional information processing relying on modern RMT design facilities for SMWM with the separation of microwave field-accumulating region and that of emission into the microprobe. Figure 16c shows geometric diagrams of RMTs for the case of local changes in sample characteristics.

The same authors achieved a spatial resolution of 1 μm [176–179]. Analysis of parameters of certain microwave microscopes [178] shows that their reconstruction (modification) may lead to a 10-fold enhancement of spatial resolution, i.e. at a level of 100 nm or possibly better.

Figure 17a displays a photograph of the experimental prototype of the scanning microwave microscope, and Fig. 17b presents an image taken by two-dimensional scanning of the profile of a microcircuit fragment (color image online).

Table 5 illustrates SMWM applications in nanotechnologies.

Table 5. Applications of microwave microscopy in nanotechnologies.

Fields of SMWM applications	Peculiarities of an SMWM
Established: • Technologies of high-temperature superconductors • Visualization of surface resistance distribution • Biology and medicine: visualization of the structure of biological objects studies and visualization of tumors	• Multifunctionality • Possibility of additional manipulation of the sample using: constant electric field magnetic field mircowave field mechanical force field
Potential: • Semiconductor micro- and nanoelectronics • Multiparametric studies of surface and near-surface layers and nanoclusters • Topological structure of electrophysical parameters of materials • Possibility of local nonthermal modification of surface and near-surface layers	• Possibility of studying the properties of subsurface layers

6.1 Operating principles of the microwave microscope

Scanning microwave microscopes are employed to explore materials at microwave frequencies and to measure changes in their resistivity [180–185].

Figure 18a presents a schematic diagram of a microwave microscope with MTs built around a coaxial line segment, and Fig. 18b shows that of an SMWM with a coaxial resonator-based MT. A microwave signal from the source enters the linear resonator with a coaxial transmission line bounded by a decoupling capacitor on the one side, and an open coaxial probe on the other. Due to multiple reflections in the coaxial resonator (with $Q \sim 10^2 - 10^3$), the signal-to-noise ratio is significantly improved and the accuracy of measurements enhanced. However, measurements at different frequencies require resonator parameters to be readjusted.

The dependence of the reflected signal on the distance to the sample is analyzed to control the probe/sample spacing. The coupling of the system to the sample is predominantly capacitive. If the sample is metallic, it forms one plate of the capacitor, while the other plate is formed by the central conductor of the coaxial probe. As the probe/sample separation decreases, the capacitance C_x increases (see inset to Fig. 18a) [185], resulting in a drop in the resonance frequency of the coaxial resonator. In one limiting case, when the probe is very far from the sample, the transmission line is open-ended and has only a terminating impedance due to fringe capacitance (C_x and C_0 in Fig. 18a). In this case, the system is a half-wave resonator with a resonance frequency f_0. In the other limiting case, when the metallic sample is in contact with the probe, there is a short circuit termination, otherwise known as a Corbino contact [186, 187]. In this case, the system is a quarter-wave resonator (Fig. 18b), and the resonance frequency is reduced by

$$\Delta f_{\max} = \frac{1}{2}\,\frac{c/2L}{\varepsilon_r^{1/2}}\,, \tag{10}$$

where c is the speed of light, L is the length of the coaxial resonator, and ε_r is the relative dielectric constant of the

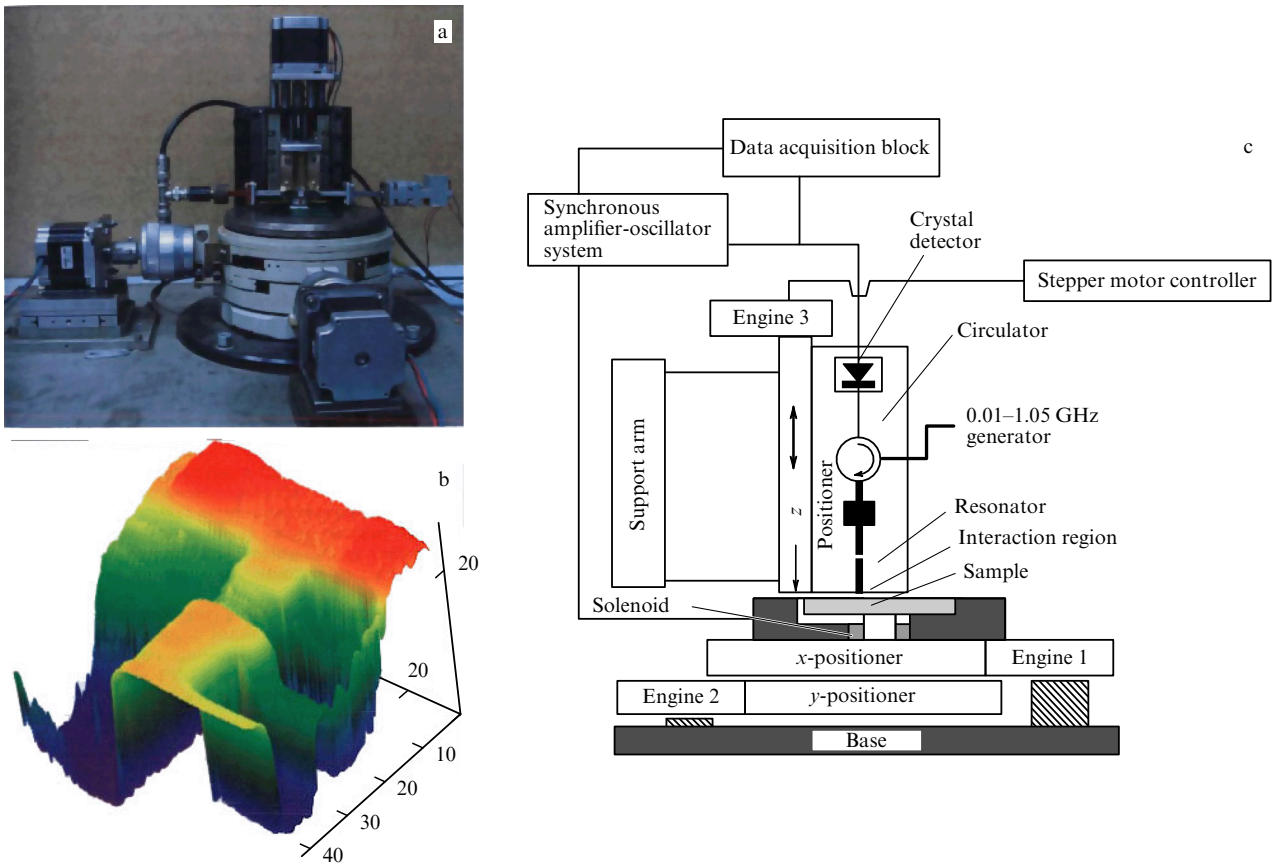

Figure 17. Microwave scanning of microstructures: (a) experimental prototype of the scanning microwave microscope; (b) result of two-dimensional scanning of the profile of a microcircuit fragment (color image online) (1 scan step — 5 μm along *x*, *y*-axes) [176, 178, 179, 207], and (c) schematic of material diagnostics with the use of a scanning microwave near-field microscope showing interaction between the open-ended coaxial probe and the sample.

coaxial cable. For the typical finite probe/sample separations, the frequency shift has values between 0 and Δf.

Currents flowing in a sample cause additional dissipation and increase radiation losses. The enhanced dissipation can be modelled by a resistance R_x between the probe/sample capacitor and the ground (see inset to Fig. 18a). The resistance has the effect of decreasing the Q factor of the coaxial resonator. As the probe moves, the capacitive gap and the plate local resistance vary, altering the resonance frequency and quality factor of the resonator. The feedback loop will keep the microwave source locked to a particular resonance frequency of the coaxial resonator [188] and thereby specify the scanning regime.

The authors of Ref. [182] used two microscopes, one operating at room temperature, the other a cryogenic microwave. The former is shown in Fig. 18c. The sample is fasten to a manual z-axis translation stage equipped with a two-axis leveling assembly. All the facility, in turn, is mounted on a motorized x-axis translation stage with a 0.1-μm step resolution. The probe is held above the sample on a motorized z-axis translation stage fixed to a rigid frame. A digital camera and binocular microscope are used to monitor the probe/sample separation during the scan. The microscope is located on a vibration-isolated table, which allows imaging with submicron resolution.

The cryogenic microscope based on the SQUID design consists of the system comprising a cryogenic xy-slider that translates the sample with approximately 1-μm accuracy, and the holder of a z-coaxial probe with a variable height. The x–y motion is achieved by computer-controlled stepper motors working at room temperature and transferring motion to the cryogenic slider through hypothermal vacuum-tight seals. The microscope can operate at temperatures between 4.2 K and room temperature.

6.2 Characteristics of the microwave microscope

6.2.1 Spatial resolution. The spatial resolution of the microscope is dictated by two linear scales (which must be significantly smaller than the wavelength for a given frequency) and may be modulated in accordance with the objective of the study. The first scale is the characteristic probe size [189, 190]. As follows from Figs 17c, 18a, c, it is given by the diameter of the central conductor of the coaxial probe or by the radius of curvature of the rod bulges of the probe gap. By using a sharp-tipped central conductor, and thus localizing more strongly the electromagnetic fields, one can reduce this length scale significantly. It should be noted that sometimes, as required by the construction, the probe is to be defined by two linear parameters.

The second important length scale is the probe/sample separation. In the system being considered, the separation is less than the radiation wavelength in a free space. However, to obtain the ultimate spatial resolution, the probe must be much closer to the surface compared with the characteristic probe size (Figs 17c, 18a–c). In principle, it is possible to establish a scanning tunneling mode to maintain a fixed height [191] or to use an atomic-force microscope operating in the contact mode [192].

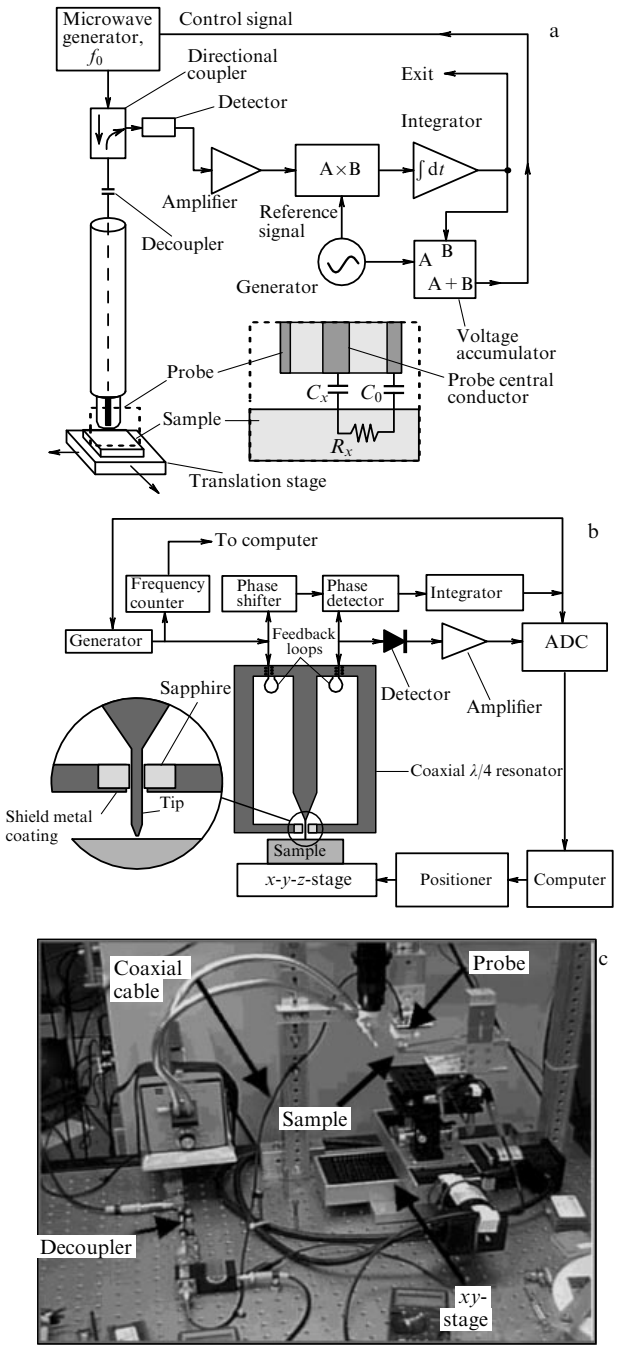

Figure 18. (a) Schematic diagram of a microwave microscope with an MT based on a coaxial line segment. (b) Schematic diagram of a microwave microscope with a coaxial resonator-based MT. (c) Room-temperature scanning near-field microwave microscope. The sample is located on the *xy*-translation stage at the right, and the probe is on the *z*-axis translation stage suspended on the frame. The coaxial resonator is controlled by a decoupler on the optical table.

We note that near-field microwave microscopy exhibits a two-order-of-magnitude lower absolute spatial resolution than near-field optical microscopy. Nevertheless, it shows a much better multiplicity in overcoming the diffraction limit (up to the factor this multiplicity can be expressed as the wavelength-to-resolution ratio). If, for example, the resolution of optical near-field microscopy ranges $(0.01–0.1)\,\lambda$, the multiplicity in overcoming the diffraction limit for scanning near-field microscopy can reach $10^4\lambda$ or more (depending on the frequency).

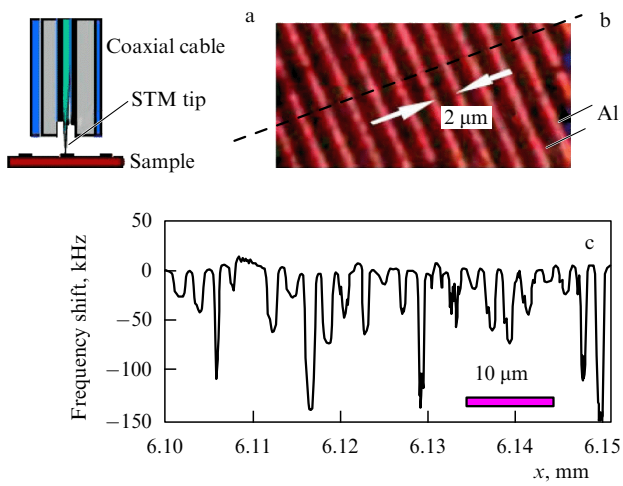

Figure 19. (Color picture online.) (a) Schematic of STM-tipped coaxial probe. (b) Optical micrograph of an infrared polarizer grid consisting of a thin Al film lined on mylar. (c) Frequency shift vs. measurement point for a scan along the dashed line in figure (b).

The best resolution was obtained for operation in the contact mode with a sharp tip instead of the central conductor of the coaxial probe. The original central conductor was removed and substituted by a hypothermal tube, and a probe tip was placed inside (see Fig. 19a) [188–190]. Using this configuration, it was possible to visualize a series of 0.5-mm wide lines in Al film deposited onto mylar (see photograph in Fig. 19b at 7.5 GHz). The lines were spaced 2 μm apart. Figure 19c shows the frequency shift scan along the dashed line shown in Fig. 19b. A marked drop in the frequency coincides with the Al lines and has a 2-μm periodicity. The variation in the signal intensity is due to intermittent contact as the probe is dragged in moving across the sample. This indicates that the microwave microscope in this configuration has a spatial resolution of better than 2 μm.

One of the advantages of the microscope under consideration is the wide dynamic range of spatial resolution. It is possible to image an entire wafer using a coaxial probe with an inner conductor diameter of 480 μm (as shown below) or very fine structures using a sharp-tipped coaxial probe. Other probe sizes can also be employed with a central conductor 200 μm, 100 μm, or 12 μm in diameter, which makes it possible to choose the spatial scale [191] and to increase the scanning rate when very high resolution is not required.

6.2.2 Frequency bandwidth. The spatial resolution of the microscope is independent of the measurement frequency, and the system can operate over a wide bandwidth. This means that maps of the surface distribution of material properties can be obtained at exactly the same frequency at which the material will be used. For example, let us consider a microscope with a coaxial resonator length $L = 2$ m. In this case, the fundamental mode frequency is approximately 50 MHz, and overtones for imaging are available at all integer multiples of 50 MHz. The upper frequency limit of the microscope is set by the operating bandwidth of the electronics. In most practical situations, a microwave source possesses an upper frequency limit at about 50 GHz. However, the microwave directional coil (connecting clutch), detector, and coaxial cable can also limit the bandwidth of the microscope. Nevertheless, it is possible to construct a microscope which has a near-continuous imaging capability over thirty frequencies between 50 MHz and 50 GHz.

6.3 Images

Surface resistance of thin $YBa_2Cu_3O_{7-\delta}$ films. Direct quantitative and nondestructive methods of analyzing superconducting ceramic samples are needed to characterize thin films that combine high spatial resolution and high scanning velocity. Moreover, the analytic facility must be constructively simple, consist of commercially available components, and provide straightforward image interpretation. The SMWM meets all these requirements.

The application of nondestructive methods of imaging microwave surface resistance has been demonstrated using various resonance probe systems. The best results of dissipation imaging in a sample were obtained by measuring the Q factor [192]. To determine the relationship between the microscope Q factor and sample surface resistance R_x, a variable-thickness aluminium thin film on a glass substrate was utilized [188]. The wedge-shaped cross section of the thin film allowed comparing variations of surface resistance with scan parameters. Using a probe with a 500-μm-diameter central conductor and selecting a resonance of the microscope at a frequency of 7.5 GHz, the authors obtained the frequency shift and Q values. The specimen was then cut into narrow strips and the local surface resistance was measured at two points. The Q factor of the microscope reaches a maximum at $R_x \to 0$; as R_x increases, Q drops due to the loss of the current induced in the sample, reaching a minimum around $R_x = 660$ Ω/sq for a height of 50 μm. Similarly, Q increases as $R_x \to \infty$ due to diminished currents in the sample [193].

To estimate the potential of the system, a thin $YBa_2Cu_3O_{7-\delta}$ (YBCO) film on a 5-cm-diameter sapphire substrate was scanned at room temperature. The thickness of the thin YBCO film varied from about 100 nm at the edges to 200 nm near the center.

The frequency shift and Q data were obtained *simultaneously* using a probe with a central conductor 500 μm in diameter and a frequency of 7.5 GHz. The scan took approximately 10 min to complete, with raster lines ~ 0.5 mm apart (*each line was 0.5 mm wide*). The authors then converted the Q data to a surface resistance image in Figs 18, 19 using the Q vs R_x calibration data at a height of 50 μm [193–195].

Figure 20a confirms that the film does indeed have a lower resistance near the center, as expected. We note that surface resistance does not show a simple radial dependence due either to variations of stoichiometry over the surface or to peculi-

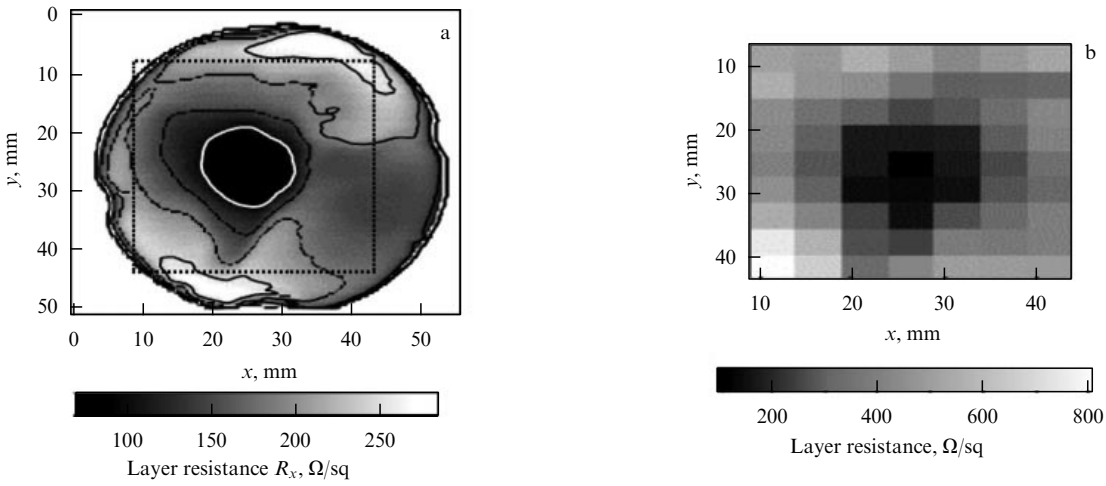

Figure 20. (a) Room-temperature distribution of surface resistance in a thin YBCO film on a 5-cm-diameter sapphire wafer. A probe with a 500-μm-diameter central conductor was used at a height of 50 μm and a frequency of 7.5 GHz. The contour lines (starting from the center) correspond to 100, 150, 200, and 250 Ω/square. DC surface resistance is shown in the dotted square. (b) Map of surface resistance of the thin YBCO film shown in figure (a).

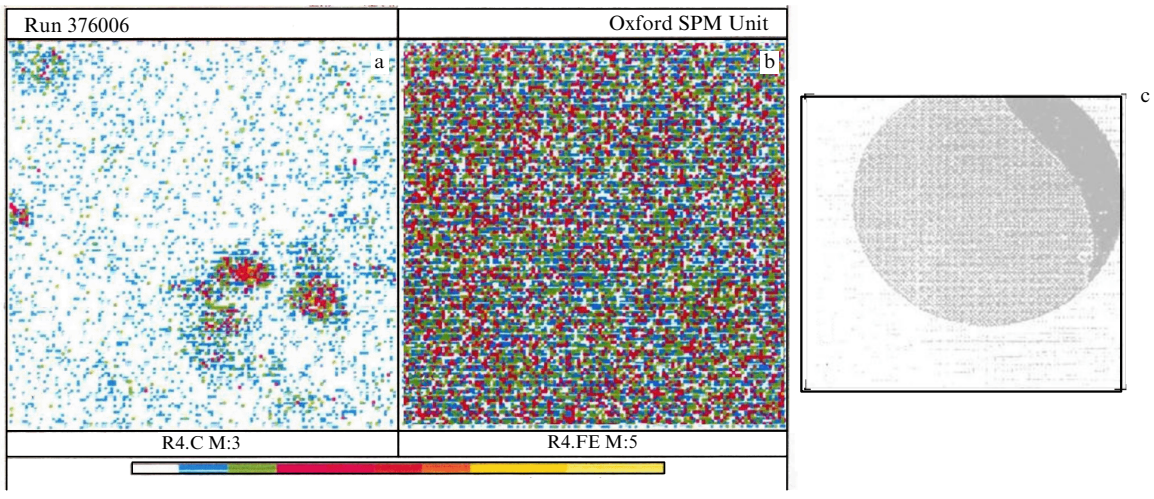

Figure 21. (Color image online.) Distribution of elements over α-Fe sample surface obtained with a microprobe (PIXE, RBS): (a) after irradiation by an electron beam (10 pulses); (b) the initial surface prior to irradiation, and (c) separated electron-irradiated region.

arities of the defective substructure. After scanning the YBCO film, the authors patterned it mechanically (which caused degradation of its surface properties) and made four-point resistance measurements all over the wafer (see Fig. 18) [195]. The DC surface resistance had a spatial dependence (Fig. 20b) identical with the microwave data in Fig. 20a [193]. However, the absolute values were approximately twice as large as the microwave results, probably due to mechanical degradation of the film during patterning [196, 197].

7. Conclusions

To conclude, certain authors have demonstrated successful application of at least several modern micro- and nanoprobes for the analysis of segregation and diffusion processes, e.g. a proton microbeam for the analysis by RBS or PIXE methods and a positron beam-based microprobe (see, for instance, Refs [198, 199]). It should be expected that a combination of complementary methods will be needed in the future to fully understand the physical nature of the processes in nanoscale objects (nanomaterials, nanocomposites), such as fatigue failure, diffusion and segregation at grain boundaries, or to diagnose multilayer systems [200]. In Refs [203, 204], α-Fe model samples doped with Al^+, C^+, or Ti^+ ions at different fluences (2×10^{17} and 5×10^{17} cm^{-2}) were utilized to analyze segregation regions of impurities (implanted ions and residual admixtures present in the chamber), including those at grain boundaries and in cluster-rich regions composed of vacancies and a few interstitial carbon atoms.

In other studies by the same authors [198, 201], it was shown that irradiation of α-Fe samples by a high-current electron beam resulted in the formation of local regions with lowered electron density, aggregates of interstitial carbon atoms, vacancies, and their agglomerations (see Figs 21, 22). Subsequent irradiation of these samples gave rise to the formation of 'craters' and thereby markedly altered the morphology of polished samples ([198, 201] and Fig. 22).

Another example of the successful application of nano- and microprobes is provided in a series of publications where seven methods were used to analyze the fatigue strength at the subatomic level in the course of studying the formation of dark spots [205–207], slip bands and speeding up chemical reactions in nanobulk materials (steel), which are accompanied by the appearance of high-temperature local regions [202, 209–212].

Worthy of note is the contribution of Russian researchers, both theorists and experimentalists, to the development of near-field microwave diagnostics of ferrites and superconducting ceramics [213–215].

Microwave diagnostics is successfully used to detect tumors and biological objects [216] and to increase the probing depth up to a few millimeters or centimeters and the probing area up to square millimeters or centimeters. In such cases, the point is visualization of an object rather than nanodefects, individual cells, or microcircuits, i.e. the depth and the area of analysis increase at the expense of object size resolution, which decreases from nanometers to millimeters or centimeters [217].

The present review does not pretend to be a comprehensive description of new, promising methods; their characteristics can be found in numerous papers and monographs. Our aim was to demonstrate the successful application of micro- and nanoprobes for diagnostics of materials at the subatomic level, bearing in mind that most of the relevant information is available only to researchers working in this specific field.

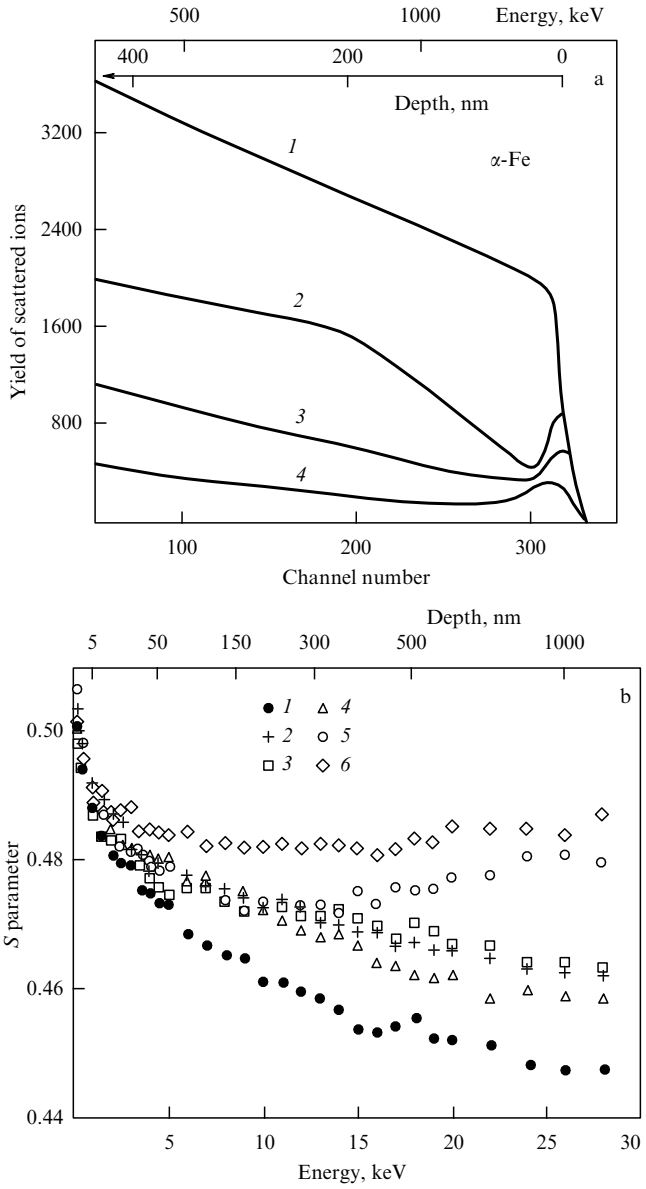

Figure 22. (a) Ion backscattering (RBS) spectra obtained with the use of a microprobe from coarse-grained α-Fe-samples (grain size 2–3 mm): *1* — before irradiation, *2* — irradiation by an electron beam with an energy density of 2.5 J cm^{-2}, *3* — irradiation by a high-current beam, 3.5 J cm^{-2}, and *4* — irradiation by a high-current beam, 5.5 J cm^{-2}. (b) Depth distribution of vacancy defects obtained using a slow beam of positrons implanted into α-Fe (positron microprobe) after irradiation by a high-current electron beam of different densities: *1* — before irradiation (grains larger than 3 μm), *2* — 2.5 J cm^{-2}, *3* — 3.5 J cm^{-2}, *4* — 4.5 J cm^{-2}, *5* — 5.2 J cm^{-2}, and *6* — 5.5 J cm^{-2}.

The data included in the review may be of value for specialists interested in the analysis and development of new nanocomposites, nanoconsolidates, and nanopolymers, as well as for those engaged in medico-biological research at the subatomic level. It is safe to predict the further development and application of analytic techniques, which promote the introduction of novel materials based on the better understanding of subatomic processes in them.

Acknowledgments. This work was performed in the framework of the Nanosystems, Nanomaterials, and Nanotechnol-

ogies Program of the National Academy of Sciences of Ukraine, Project F41/20-2011 of the Ukrainian SFBR, and joint Project T11K-058 of the Belarussian FBR.

The authors are grateful to researchers of the Institute of Applied Physics, National Academy of Sciences of Ukraine, Sumy, and N I Slipchenko (Kharkiv National Radiotechnical Institute) for courteous permission to use the results of their works. Our thanks are also due to R Krause-Rehberg and W Triftshäuser, Germany, who kindly provided us with the materials of their research and the future book.

References

1. Vijayakumar M et al. *Def. Sci. J.* **39** (1) 13 (1989)
2. Elovikov S S *Sorosovskii Obraz. Zh.* (2) 82 (2001)
3. Cadel E, Fraczkiewicz A, Blavette D *Annu. Rev. Mater. Res.* **33** 215 (2003)
4. Chisholm M F, Pennycook S J *Philos. Mag.* **86** 4699 (2006)
5. Cherepin V T *Ionnyi Mikrozondovyi Analiz* (Ion Microprobe Analysis) (Kiev: Nauk. Dumka, 1992)
6. Reyntjens S, Puers R *J. Micromech. Microeng.* **11** 287 (2001)
7. Watt F, Grime G W (Eds) *Principles and Applications of High-Energy Microbeams* (Bristol: A. Hilger, 1987)
8. Maggiore C J *Scanning Electron Microsc.* **1** 419 (1980)
9. Breese M B H, Jamieson D N, King P J C *Materials Analysis Using a Nuclear Microprobe* (New York: John Wiley, 1996)
10. Shibata H et al. *Nucl. Instrum. Meth. Phys. Res. B* **260** 321 (2007)
11. Raepsaet C et al. *Nucl. Instrum. Meth. Phys. Res. B* **267** 2245 (2009)
12. Takai M *Nucl. Instrum. Meth. Phys. Res. B* **113** 330 (1996)
13. Sie S H *Nucl. Instrum. Meth. Phys. Res. B* **130** 592 (1997)
14. Przybylowicz W J et al. *Nucl. Instrum. Meth. Phys. Res. B* **130** 335 (1997)
15. Vis R D *The Proton Microprobe*: *Applications in Biomedical Field* (Boca Raton, Fla.: CRC Press, 1985)
16. Moretto Ph, Llabador Y *Nucl. Instrum. Meth. Phys. Res. B* **130** 324 (1997)
17. Llabador Y, Moretto Ph *Applications of Nuclear Microprobes in the Life Sciences*: *An Efficient Analytical Technique for Research in Biology and Medicine* (Singapore: World Scientific, 1998)
18. Demortier G *Nucl. Instrum. Meth. Phys. Res. B* **113** 347 (1996)
19. Malmqvist K G *Nucl. Instrum. Meth. Phys. Res. B* **113** 336 (1996)
20. Kertész Zs et al. *Nucl. Instrum. Meth. Phys. Res. B* **267** 2236 (2009)
21. Meijer J et al. *Nucl. Instrum. Meth. Phys. Res. B* **161 – 163** 898 (2000)
22. Röcken H et al. *Nucl. Instrum. Meth. Phys. Res. B* **181** 274 (2001)
23. Watt F et al. *Int. J. Nanosci.* **4** 269 (2005)
24. Ponomarev A G *Visn. Sum. DU Ser. Fiz., Mat., Mekh.* (2) 46 (2008)
25. Watt F et al. *Mater. Today* **10** (6) 20 (2007)
26. Ziegler J F, Ziegler M D, Biersack J P *Nucl. Instrum. Meth. Phys. Res. B* **268** 1818 (2010); "SRIM — The stopping and range of ions in matter", http://www.SRIM.org/
27. Teo E J et al. *Proc. SPIE* **5347** 264 (2004)
28. Legge G J F *Nucl. Instrum. Meth. Phys. Res. B* **130** 9 (1997)
29. Val'ter A K (Ed.) *Elektrostaticheskie Uskoriteli Zaryazhennykh Chastits* (Electrostatic Accelerators of Charged Particles) (Moscow: Gosatomizdat, 1963)
30. Teo E J et al. *J. Vac. Sci. Technol. B* **22** 560 (2004)
31. Udalagama C N B et al. *Nucl. Instrum. Meth. Phys. Res. B* **260** 390 (2007)
32. Schroeder J B, Howell C W, Norton G A *Nucl. Instrum. Meth. Phys. Res. B* **24 – 25** 763 (1987)
33. Ferry J A *Nucl. Instrum. Meth. Phys. Res. A* **328** 28 (1993)
34. Gol'din L L *Fizika Uskoritelei* (Physics of Accelerators) (Moscow: Nauka, 1983)
35. Mous D J W et al. *Nucl. Instrum. Meth. Phys. Res. B* **130** 31 (1997)
36. Mordyk S M et al. *Rev. Sci. Instrum.* **75** 1922 (2004)
37. Mordyk S M et al. *Nucl. Instrum. Meth. Phys. Res. B* **231** 37 (2005)
38. Miroshnichenko V et al. *Nucl. Instrum. Meth. Phys. Res. B* **260** 39 (2007)
39. Adamczewski J et al. *Nucl. Instrum. Meth. Phys. Res. B* **130** 57 (1997)
40. Kalbitzer S *Nucl. Instrum. Meth. Phys. Res. B* **158** 53 (1999)
41. Allan G L, Legge G J F, Zhu J *Nucl. Instrum. Meth. Phys. Res. B* **34** 122 (1988)
42. Legge G J F et al. *Rev. Sci. Instrum.* **67** 909 (1996)
43. Colman R A, Legge G J F *Nucl. Instrum. Meth. Phys. Res. B* **73** 561 (1993)
44. Vis R D et al. *Nucl. Instrum. Meth. Phys. Res. B* **197** 179 (1982)
45. Kurashima S et al. *Nucl. Instrum. Meth. Phys. Res. B* **260** 65 (2007)
46. Kurashima S et al. *Nucl. Instrum. Meth. Phys. Res. B* **267** 2024 (2009)
47. Pierce T B, Peck P F, Cuff D R A *Nature* **211** 66 (1966)
48. Mak B W, Bird J R, Sabine T M *Nature* **211** 738 (1966)
49. Maggiore C J *Nucl. Instrum. Meth. Phys. Res. B* **191** 199 (1981)
50. Meijer J et al. *Nucl. Instrum. Meth. Phys. Res. B* **99** 423 (1995)
51. Stephan A et al. *Nucl. Instrum. Meth. Phys. Res. B* **113** 387 (1996)
52. Hawkes P W *Quadrupoles in Electron Lens Design* (New York: Academic Press, 1970)
53. Yavor S Ya *Fokusirovka Zaryazhennykh Chastits Kvadrupol'nymi Linzami* (Focusing Charge Particles with Quadrupole Lenses) (Moscow: Atomizdat, 1968)
54. Dymnikov A D, Yavor S Ya *Zh. Tekh. Fiz.* **33** 7851 (1963)
55. Dymnikov A D et al. *Zh. Tekh. Fiz.* **35** 3431 (1965)
56. Cookson J A, Ferguson A T G, Pilling F D *J. Radioanalytical Chem.* **12** 39 (1972)
57. Ryabchikov A I, Puzyrevich A G *Prib. Tekh. Eksp.* (5) 209 (1990)
58. Bondarenko V N, Goncharov A V, Kolot V Ya *Vopr. Atom. Nauki Tekh. Yad.-Fiz. Issled.* (4) 08 (1999)
59. Ponomarev A G et al. *Priklad. Fiz.* (2) 28 (2008)
60. Magilin D V et al. *Nucl. Instrum. Meth. Phys. Res. B* **267** 2046 (2009)
61. Rebrov V A et al. *Nucl. Instrum. Meth. Phys. Res. B* **260** 34 (2007)
62. Ponomarev A G et al. *Nucl. Instrum. Meth. Phys. Res. B* **201** 637 (2003)
63. Ponomarev A G, Miroshnichenko V I, Storizhko V E *Nucl. Instrum. Meth. Phys. Res. A* **506** 20 (2003)
64. Matsuyama S et al. *Nucl. Instrum. Meth. Phys. Res. B* **260** 55 (2007)
65. Grime G W, Watt F *Beam Optics of Quadrupole Probe-Forming Systems* (Bristol: A. Hilger, 1984)
66. Watt F et al. *Nucl. Instrum. Meth. Phys. Res. B* **210** 14 (2003)
67. Brazhnik V et al. *Nucl. Instrum. Meth. Phys. Res. B* **77** 29 (1993)
68. Brazhnik V A et al. *Nucl. Instrum. Meth. Phys. Res. B* **104** 92 (1995)
69. Moloney G R, Jamieson D N, Legge G J F *Nucl. Instrum. Meth. Phys. Res. B* **54** 68 (1991)
70. Dymnikov A D, Jamieson D N, Legge G J F *Nucl. Instrum. Meth. Phys. Res. B* **104** 64 (1995)
71. Butz T, Legge G J F *Nucl. Instrum. Meth. Phys. Res. B* **113** 317 (1996)
72. Butz T et al. *Nucl. Instrum. Meth. Phys. Res. B* **161 – 163** 323 (2000)
73. Ryan C G et al. *Nucl. Instrum. Meth. Phys. Res. B* **158** 18 (1999)
74. Ryan C G, Jamieson D N *Nucl. Instrum. Meth. Phys. Res. B* **158** 97 (1999)
75. Breese M B H et al. *Nucl. Instrum. Meth. Phys. Res. B* **158** 48 (1999)
76. Ryan C G et al. *Nucl. Instrum. Meth. Phys. Res. B* **181** 12 (2001)
77. Datzmann G et al. *Nucl. Instrum. Meth. Phys. Res. B* **158** 74 (1999)
78. Glass G A et al. *MRS Proc.* **908** 0908-OO06-01 (2006)
79. Johansson S A E, Campbell J L, Malmqist K G (Eds) *Particle-Induced X-Ray Emission Spectrometry* (*PIXE*) (New York: Wiley, 1995)
80. Johansson S A E, Campbell J L *PIXE*: *a Novel Technique for Elemental Analysis* (Chichester: Wiley, 1988)
81. *Intercomparison of PIXE Spectrometry Software Packages* (IAEA-TECDOC-1342) (Vienna: IAEA, 2003)
82. Ryan C G, van Achterbergh E, Jamieson D N *Nucl. Instrum. Meth. Phys. Res. B* **231** 162 (2005)
83. Ryan C G et al. *Nucl. Instrum. Meth. Phys. Res. B* **260** 1 (2007)
84. Ryan C G et al. *Nucl. Instrum. Meth. Phys. Res. B* **268** 1899 (2010)
85. Watt F et al. *Nucl. Instrum. Meth. Phys. Res. B* **181** 431 (2001)
86. Barapatre N et al. *Nucl. Instrum. Meth. Phys. Res. B* **268** 2156 (2010)
87. Andrea T et al. *Nucl. Instrum. Meth. Phys. Res. B* **268** 1884 (2010)
88. Shipatov E T *Obratnoe Rasseyanie Bystrykh Ionov*: *Teoriya, Eksperiment, Praktika* (Backscattering of Fast Ions: Theory, Experiment, Practice) (Rostov-on-Don: Izd. Rostovskogo Univ., 1988)

89. Tesmer J R, Nastasi M (Eds) *Handbook of Modern Ion Beam Materials Analysis* (Pittsburgh, Pa.: Materials Research Society, 1995)
90. Molodtsov S L, Gurbich A F, Jeynes C *J. Phys. D* **41** 205303 (2008)
91. Barradas N P et al. *Nucl. Instrum. Meth. Phys. Res. B* **266** 1338 (2008)
92. Samlenski R et al. *Nucl. Instrum. Meth. Phys. Res. B* **190** 324 (2002)
93. Llabador Y, Moretto Ph, Guegan H *Nucl. Instrum. Meth. Phys. Res. B* **77** 123 (1993)
94. Sjöland K A et al. *Nucl. Instrum. Meth. Phys. Res. B* **130** 20 (1997)
95. Breese M B H et al. *Nucl. Instrum. Meth. Phys. Res. B* **264** 345 (2007)
96. Vizkelethy G et al. *Nucl. Instrum. Meth. Phys. Res. B* **260** 264 (2007)
97. Colombo E et al. *Nucl. Instrum. Meth. Phys. Res. B* **267** 2181 (2009)
98. Vizkelethy G et al. *Nucl. Instrum. Meth. Phys. Res. B* **267** 2185 (2009)
99. Huddle J R et al. *Nucl. Instrum. Meth. Phys. Res. B* **261** 475 (2007)
100. Rossi P et al. *Nucl. Instrum. Meth. Phys. Res. B* **181** 437 (2001)
101. Mathis F et al. *Nucl. Instrum. Meth. Phys. Res. B* **268** 2078 (2010)
102. Manfredotti C et al. *Nucl. Instrum. Meth. Phys. Res. B* **136–138** 1333 (1998)
103. Zhdankin V *Sovrem. Tekhnol. Avtomatizatsii* (3) 6 (2005)
104. Schrimpf R D et al. *Nucl. Instrum. Meth. Phys. Res. B* **261** 1133 (2007)
105. Fischer B E et al. *Nucl. Instrum. Meth. Phys. Res. B* **158** 245 (1999)
106. Cholewa M et al. *Nucl. Instrum. Meth. Phys. Res. B* **130** 275 (1997)
107. Kamiya T, Hirao T, Kobayashi Y *Nucl. Instrum. Meth. Phys. Res. B* **219–220** 1010 (2004)
108. Reed R A et al. *Nucl. Instrum. Meth. Phys. Res. B* **261** 443 (2007)
109. Vizkelethy G et al. *Nucl. Instrum. Meth. Phys. Res. B* **268** 2092 (2010)
110. Barberet Ph et al. *Nucl. Instrum. Meth. Phys. Res. B* **267** 2003 (2009)
111. Khodja H et al. *Nucl. Instrum. Meth. Phys. Res. B* **267** 1999 (2009)
112. Arteaga-Marrero N et al. *Nucl. Instrum. Meth. Phys. Res. B* **260** 91 (2007)
113. Kirkby K J et al. *Nucl. Instrum. Meth. Phys. Res. B* **260** 97 (2007)
114. Kobayashi Y et al. *Nucl. Instrum. Meth. Phys. Res. B* **210** 308 (2003)
115. Imaseki H et al. *Nucl. Instrum. Meth. Phys. Res. B* **260** 81 (2007)
116. Konishi T et al. *Nucl. Instrum. Meth. Phys. Res. B* **267** 2171 (2009)
117. Springham S V et al. *Nucl. Instrum. Meth. Phys. Res. B* **130** 155 (1997)
118. van Kan J A et al. *Nucl. Instrum. Meth. Phys. Res. B* **148** 1085 (1999)
119. Watt F *Nucl. Instrum. Meth. Phys. Res. B* **158** 165 (1999)
120. van Kan J A et al. *Nucl. Instrum. Meth. Phys. Res. B* **161–163** 366 (2000)
121. Chiam C Y et al. *Nucl. Instrum. Meth. Phys. Res. B* **260** 455 (2007)
122. van Kan J A, Bettiol A A, Watt F *Appl. Phys. Lett.* **8**3 1629 (2003)
123. van Kan J A, Bettiol A A, Watt F *Nucl. Instrum. Meth. Phys. Res. B* **181** 258 (2001)
124. Menzel F et al. *Nucl. Instrum. Meth. Phys. Res. B* **231** 372 (2005)
125. Rajta I et al. *Nucl. Instrum. Meth. Phys. Res. B* **267** 2292 (2009)
126. van Kan J A et al. *Nucl. Instrum. Meth. Phys. Res. B* **260** 460 (2007)
127. van Kan J A, Bettiol A A, Watt F *Nano Lett.* **6** 579 (2006)
128. Furuta Y et al. *Nucl. Instrum. Meth. Phys. Res. B* **267** 2285 (2009)
129. Ansari K et al. *Appl. Phys. Lett.* **85** 476 (2004)
130. Ansari K et al. *J. Micromech. Microeng.* **16** 1967 (2006)
131. van Kan J A et al. *Int. J. Nanotechnol.* **1** 464 (2004)
132. Sum T C et al. *Nucl. Instrum. Meth. Phys. Res. B* **210** 266 (2003)
133. Krause-Rehberg R, Leipner H S *Positron Annihilation in Semiconductors*: *Defect Studies* (Berlin: Springer-Verlag, 1999)
134. Triftshäuser W, in *Microscopic Methods in Metals* (Ed. U Gonser) (Berlin: Springer-Verlag, 1986) p. 249
135. Pogrebnjak A D, Beresnev V M, in *Nanocoatings, Nanosystems and Nanotechnologies* (Ed. A Pogrebnjak) (New York: Bentham Science Publ., 2012) p. 290
136. Vehanen A et al. *Appl. Phys. A* **32** 163 (1983)
137. Vehanen A et al., in *Positron Annihilation* (Eds L Dorikens-Vanpraet, D Segers) (Singapore: World Scientific, 1989) p. 39
138. Vehanen A et al. *Phys. Rev. B* **35** 4606 (1987)
139. Brusa R S et al. *Mater. Sci. Forum* **105–110** 1849 (1992)
140. Bauer-Kugelman W et al. *Mater. Sci. Forum* **255–257** 662 (1997)
141. Beling C D et al. *Appl. Phys. A* **42** 111 (1987)
142. Fisher D A, Lynn K G, Gidley D W *Phys. Rev. B* **33** 4479 (1986)
143. Kögel G *Appl. Phys. A* **63** 227 (1996)
144. Kögel G et al. *Phys. Rev. Lett.* **60** 1550 (1988)
145. Akahane T et al. *Appl. Phys. A* **51** 146 (1990)
146. Valkealahti S, Niemien R M *Appl. Phys. A* **32** 95 (1983)
147. Valkealahti S, Niemien R M *Appl. Phys. A* **35** 51 (1984)
148. Ghosh V J *Appl. Surf. Sci.* **85** 187 (1995)
149. Makhov A F *Fiz. Tverd. Tela* **2** 2164 (1960) [*Sov. Phys. Solid State* **2** 1934 (1961)]
150. Ghosh V J, Aers G C *Phys. Rev. B* **51** 45 (1995)
151. Gebauer J et al. *Mater. Sci. Forum* **255–257** 204 (1997)
152. Schultz P J, Lynn K G *Rev. Mod. Phys.* **60** 701 (1988)
153. Schödlbauer D et al. *Nucl. Instrum. Meth. Phys. Res. B* **34** 258 (1988)
154. Suzuki R et al. *Jpn. J. Appl. Phys.* **30** L532 (1991)
155. Willutzki P et al. *Meas. Sci. Technol.* **5** 548 (1994)
156. Coleman P G, Baker J A, Chilton N B *Mater. Sci. Forum* **105–110** 213 (1992)
157. Mills A P J, Gullikson E M *Appl. Phys. Lett.* **49** 1121 (1986)
158. Bauer-Kugelmann W et al. *Appl. Surf. Sci.* **116** 231 (1997)
159. Duffy J A et al. *Appl. Surf. Sci.* **116** 241 (1997)
160. Pensl G, Helbig R *Adv. Solid State Phys.* **30** 133 (1990)
161. Muehlhoff L et al. *J. Appl. Phys.* **60** 2842 (1986)
162. Sonntag H, Kalbitzer S *Appl. Phys. A* **61** 363 (1995)
163. Brauer G et al. *Phys. Rev. B* **54** 3084 (1996)
164. Uhlmann K et al. *Analyt. Chem.* **353** 594 (1995)
165. Zecca A et al. *Europhys. Lett.* **29** 617 (1995)
166. Triftshäuser W et al. *Nucl. Instrum. Meth. Phys. Res. B* **130** 264 (1997)
167. Triftshäuser G et al. *Appl. Surf. Sci.* **116** 45 (1997)
168. Uhlmann K, Britton D T, Kögel G *Meas. Sci. Technol.* **6** 932 (1995)
169. Uhlmann K, Britton D T, Kögel G *Optik* **98** 5 (1994)
170. Canter K F et al., in *Atomic Physics with Positrons* (Eds J W Humberston, E A G Armour) (New York: Plenum Press, 1987) p. 153
171. Triftshäuser W, in *Proc. of the Intern. Workshop on Advanced Techniques of Positron Beam Generation and Control, JAERI, Japan, 1998*, p. 57
172. Pogrebnjak A D et al. *Phys. Lett. A* **265** 225 (2000)
173. Pogrebnjak A D et al. *Phys. Lett. A* **241** 357 (1998)
174. Pogrebnjak A D et al. *Usp. Fiz. Nauk* **179** 35 (2009) [*Phys. Usp.* **52** 29 (2009)]
175. Gordienko Yu E, Slipchenko N I, Petrov V V *Radioelektron. Informatika* (3) 19 (2007)
176. Slipchenko N I "Fizichni osnovi blizhn'opol'ovoi NVCh diagnostiki materialiv i seredovishch" ("Physical basis of near-field UHF diagnostics of materials and media"), Doctoral Thesis Phys.-Math. Sci. (Sumy, 2008)
177. Gordienko Yu E et al. "Algoritm rekonstruktsii izobrazhenii v blizhnepolevoi skaniruyushchei mikroskopii" ("Algorithm of image reconstruction in near-field scanning microscopy"), in *Radiotekh. Vseukr. Mezhved. Nauch.-Tekh. Sb.* (2003) p. 135
178. Gordienko Yu E et al., in *3-ya Mezhdunarod. Naukovo-Tekhnichna Konf. "Sensorna Elektronika ta Mikrosistemni Tekhnologii", Ukraina, Odessa, 2-6 Chervnya 2008*, p. 156
179. Ryabukhin O O, Gordienko Y O, Slipchenko N I "Integral'nii mikropolozkovii rezonatornii zond mikrokhvil'ovogo mikroskopa" ("Integrated microslider resonator microprobe of the microwave microscope"), Dekl. Patent No. 71456A, appr. 15.11.2004
180. Ash E A, Nicholls G *Nature* **237** 510 (1972)
181. Bryant C A, Gunn J B *Rev. Sci. Instrum.* **36** 1614 (1965)
182. Fee M, Chu S, Hänsch T W *Opt. Commun.* **69** 219 (1989)
183. Wei T et al. *Appl. Phys. Lett.* **68** 3506 (1996)
184. Golosovsky M, Davidov D *Appl. Phys. Lett.* **68** 1579 (1996)
185. Vlahacos C P et al. *Appl. Phys. Lett.* **69** 3272 (1996)
186. Booth J C et al. *Rev. Sci. Instrum.* **65** 2082 (1994)
187. Steinhauer D E et al. *Appl. Phys. Lett.* **71** 1736 (1997)
188. Anlage S M et al. *IEEE Trans. Appl. Supercond.* **7** 3686 (1997)
189. Stranick S J, Weiss P S *Rev. Sci. Instrum.* **64** 1232 (1993)
190. Stranick S J, Weiss P S *Rev. Sci. Instrum.* **65** 918 (1994)
191. Van der Weide D W, Neuzil P *J. Vac. Sci. Technol. B* **14** 4144 (1996)
192. Steinhauer D E et al. *Appl. Phys. Lett.* **72** 861 (1998)
193. Vlahacos C P et al. *Appl. Phys. Lett.* **72** 1778 (1998)
194. Feenstra B J et al. *IEEE MTT-S Int. Microwave Symp. Digest* 965 (1998)

195. Pogrebnjak A D, Tyurin Yu N *Usp. Fiz. Nauk* **175** 515 (2005) [*Phys. Usp.* **48** 487 (2005)]
196. Boiko V I, Valyaev A N, Pogrebnyak A D *Usp. Fiz Nauk* **169** 1243 (1999) [*Phys. Usp.* **42** 1139 (1999)]
197. Pogrebnjak A D et al. *Struktura i Svoistva Nanokompozitnykh Gibridnykh i Polimernykh Pokrytii* (The Structure and Properties of Nanocomposite Hybrid Coatings) (Moscow: URSS, 2011)
198. Grafutin V I, Prokop'ev E P *Usp. Fiz. Nauk* **172** 67 (2002) [*Phys. Usp.* **45** 59 (2002)]
199. Lavrent'ev V I, Pogrebnyak A D, Sandrik R *Pis'ma Zh. Eksp. Teor. Fiz.* **65** 618 (1997) [*JETP Lett.* **65** 651 (1997)]
200. Pogrebnjak A D, Shpak A P, Beresnev V M, in *New Nanotechniques* (Eds A Malik, R J Rawat) (New York: Nova Science Publ., 2009) p. 687
201. Haaks M *CIRP Ann. Manufact. Technol.* **57** 537 (2008)
202. Lavrent'ev V I et al. *Pis'ma Zh. Tekh. Fiz.* **24** (9) 13 (1998) [*Tech. Phys. Lett.* **24** 334 (1998)]
203. Lavrent'ev V I, Pogrebnyak A D, Sandrik R *Pis'ma Zh. Eksp. Teor. Fiz.* **24** 91 (1997) [*JETP Lett.* **65** 91 (1997)]
204. Shpak A D, Kunitskii Yu A, Karbovskii V L *Klasternye i Nanostrukturnye Materialy* (Cluster and Nanostructural Materials) (Kiev: Akademperiodika, 2001)
205. Shpak A D, Kunitskii Yu A, Smik S Yu *Diagnostika Nanosistem* (Diagnostics of Nanosystems) (Kiev: Akademperiodika, 2003) Chs 1, 2
206. Gomza Yu P et al. *Nanosist. Nanomater. Nanotekhnol.* **7** (2) 411 (2009)
207. Azarenkov N A et al. *Fiz. Inzheneriya Poverkhn.* **3** (1–2) 127 (2005)
208. Gorbachev L A, Pogrebnjak A D *Metallofiz. Noveishie Tekhnol.* **32** (1) 121 (2010)
209. Cherenda N et al. *Plasma Process. Polymers* **6** 178 (2009)
210. Pogrebnyak A D et al. *Pis'ma Zh. Tekh. Fiz.* **35** (19) 103 (2009) [*Tech. Phys. Lett.* **35** 925 (2009)]
211. Pogrebnyak A D et al. *Izv. Vyssh. Ucheb. Zaved. Fiz.* (12) 61 (2009) [*Russ. Phys. J.* **52** 1317 (2009)]
212. Volopilkin E A, Parafin A E, Reznik A N *Zh. Tekh. Fiz.* **70** (2) 74 (2000) [*Tech. Phys.* **45** 214 (2000)]
213. Semenov A A et al. *Zh. Tekh. Fiz.* **71** (10) 13 (2001) [*Tech. Phys.* **46** 1218 (2001)]
214. Reznik A N, Yurasova N V *Zh. Tekh. Fiz.* **74** (4) 108 (2004) [*Tech. Phys.* **49** 485 (2004)]
215. Tabib-Arat M, Katz J V, LeClair S R *IEEE Trans. Instrum. Meas.* **48** 1111 (1999)
216. Steinhauer D E, Anlage S M *J. Appl. Phys.* **89** 2314 (2001)
217. Lee S-C, Anlage S M *Appl. Phys. Lett.* **82** 1893 (2003)